Article

Chicxulub impact winter sustained by fine silicate dust

Check for updates

Cem Berk Senel [1,2] ✉, Pim Kaskes [2,9], Orkun Temel[1,3,9], Johan Vellekoop [4,5], Steven Goderis [2], Robert DePalma[6,7], Maarten A. Prins [8], Philippe Claeys [2] & Özgür Karatekin[1]

The Chicxulub impact is thought to have triggered a global winter at the Cretaceous-Palaeogene (K-Pg) boundary 66 million years ago. Yet the climatic consequences of the various debris injected into the atmosphere following the Chicxulub impact remain unclear, and the exact killing mechanisms of the K-Pg mass extinction remain poorly constrained. Here we present palaeoclimate simulations based on sedimentological constraints from an expanded terrestrial K-Pg boundary deposit in North Dakota, United States, to evaluate the relative and combined effects of impact-generated silicate dust and sulfur, as well as soot from wildfires, on the post-impact climate. The measured volumetric size distribution of silicate dust suggests a larger contribution of fine dust (~0.8–8.0 μm) than previously appreciated. Our simulations of the atmospheric injection of such a plume of micrometre-sized silicate dust suggest a long atmospheric lifetime of 15yr, contributing to a global-average surface temperature falling by as much as 15°C. Simulated changes in photosynthetic active solar radiation support a dust-induced photosynthetic shut-down for almost 2 yr post-impact. We suggest that, together with additional cooling contributions from soot and sulfur, this is consistent with the catastrophic collapse of primary productivity in the aftermath of the Chicxulub impact.

The Chicxulub asteroid impact event ~66 million years ago showcases a unique opportunity to examine the rate, magnitude and mechanisms of extreme and abrupt climate change in Earth's history[1–4]. The 45–60° inclined impact of a 10- to 15-km-sized carbonaceous chondrite on the Yucatán Peninsula in Mexico[5,6] triggered a chain reaction of events ultimately responsible for the Cretaceous-Palaeogene (K-Pg) mass extinction and the demise of ~75% of species, including the iconic non-avian dinosaurs[4,7]. Early studies have suggested that ejecta release of crater material into the higher atmosphere[2,8–10], as derived from the shock-vaporization of the Yucatán target stratigraphy consisting of a

carbonate and evaporite platform on top of a granitic basement[11,12] (Fig. 1), triggered a global impact winter, leading to a dramatic decrease in global annual mean surface temperature by more than 10 °C in the first year(s) after the impact[2,3,10,13–16].

More-recent Chicxulub palaeoclimate modelling studies[10,17–19] investigated with increased detail the short-term climatic effects of atmospheric injections of fine-grained ejecta, which we define as a group of impact-generated material ejected out of the impact structure and characterized by a dominant grain size of generally <10 μm. For the Chicxulub case, fine-grained ejecta consist largely of three

[1]Reference Systems and Planetology Department, Royal Observatory of Belgium, Brussels, Belgium. [2]Archaeology, Environmental Changes & Geo-chemistry (AMGC), Vrije Universiteit Brussel, Brussels, Belgium. [3]Institute of Astronomy, KU Leuven, Leuven, Belgium. [4]Division of Geology, KU Leuven, Leuven, Belgium. [5]Operational Directorate Earth and History of Life, Royal Belgian Institute for Natural Sciences, Brussels, Belgium. [6]Department of Earth and Environmental Sciences, University of Manchester, Manchester, UK. [7]Department of Geosciences, Florida Atlantic University, Boca Raton, FL, USA. [8]Department of Earth Sciences, Vrije Universiteit Amsterdam, Amsterdam, the Netherlands. [9]These authors contributed equally: Pim Kaskes, Orkun Temel. ✉e-mail: cem.berk@observatory.be
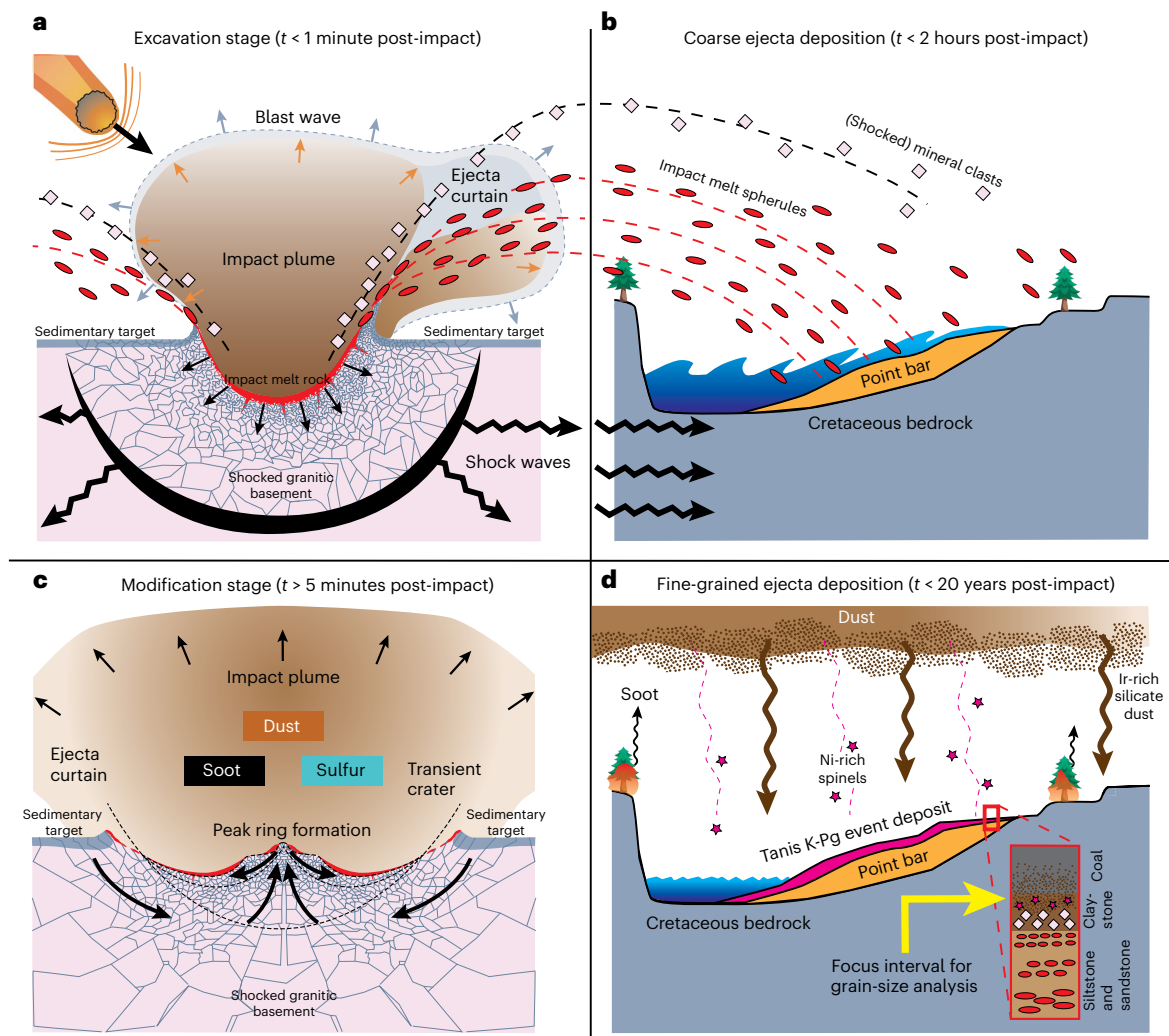
Fig. 1 | Conceptual model of the Chicxulub impact plume showing different stages of production, transport and deposition of coarse and fine-grained impact-generated ejecta (not to scale). a, Chicxulub impact site, Yucatán Peninsula, Mexico. The excavation stage shows a 45° impact of a 10- to 15-km-sized bolide from the northeast[5]. The Yucatán target rocks are displaced to form a transient cavity with an uplifted rim and are ejected within an impact plume and ejecta curtain[10]. Glassy impact melt spherules[36] and shocked minerals from the granitic basement[9] are rapidly expelled out of the crater. **b**, At the terrestrial Tanis K-Pg site[41] in North Dakota (United States), ~3,000 km north of Chicxulub, rapidly moving impact-induced shock waves trigger a seiche-inundation event on top of a riverine point bar deposit. Meanwhile, the melt spherules are−largely ballistically−emplaced in the event deposit, followed by the arrival of shocked mineral clasts, constraining the time of deposition at <2 h after impact[9,31]. **c**, At the impact site, in the minutes after the excavation

stage, the cavity rim collapses whereas rocks in the central area are first uplifted and then subside downwards and outwards to form a peak ring[10]. Meanwhile, the impact plume with fine-grained ejecta (silicate dust, soot and sulfate particles from S-bearing gases) grows, expands and rises into the stratosphere, thereby distributing material around the globe[10]. **d**, At Tanis, in the first years post-impact, atmospheric settling is taking over with Ni-rich spinel-bearing spherules, soot particles derived from wildfires and a large fraction of silicate dust[41]. The panel shows a schematic stratigraphy of a silt-to-sandstone interval with glassy spherules, followed by claystone with shocked minerals, Ni-rich spinels and fine dust rich in iridium, overlain by a lignite[41]. The claystone interval just below the Palaeogene coal is the main focus in this study[49,50]. Panels **a,c** adapted with permission from ref. 10, Springer Nature Limited. Credit: tree icon, Flaticon.com.

groups (Fig. 1c): (1) sulfur-bearing particles produced by water and sulfur-bearing gases, resulting from shock-vaporized evaporites[8,16], (2) soot particles, probably generated from burning of organic-rich target rocks and release from global wildfires[20–23] and (3) silicate dust particles, derived from pulverization of the Yucatán crystalline basement[24,25]. Besides these fine-grained ejecta, the collision also released other products from the Yucatán target area into the atmosphere, such as carbon dioxide, water vapour and methane[16]. Elevated concentrations of these climate-active gases resulted, after the initial impact winter[14], in global warming[3,10,14]; CO_2 also played a key role in post-impact ocean acidification and primary productivity[26]. However, these products were acting predominantly on a much longer timescale

(in the order of thousands to tens of thousands of years[10,26]) than considered in this palaeoclimate study.

The emitted mass and particle properties of impact-generated sulfur, soot and dust remain relatively poorly constrained to date. Therefore, many uncertainties remain surrounding the atmospheric lifetime of fine-grained ejecta and their short-term climatic effects, which in part result from a limited amount of observational data from K-Pg boundaries incorporated in palaeoclimate models. Moreover, no combined palaeoclimate scenario emitting concurrently all fine-grained ejecta components has been considered so far for the Chicxulub case[10]. Quantifying relative and combined roles of these fine-grained ejecta on the global K-Pg climate crisis is paramount to better understand

the severity and duration of the K-Pg impact winter and to identify the killing mechanisms responsible for the mass extinction.

The K-Pg impact winter hypothesis, proposed originally in 1980[2], was centred around dust-sized material ejected from the crater into the stratosphere and subsequently spread around the globe[3]. However, this dust scenario was rejected in the early 2000s because the fraction and mass of this clastic debris at the K-Pg boundary was estimated to be too modest to cause an impact winter[27]. Alternative studies pointed out that the post-impact sulfur release constituted a more important driver behind the prolonged K-Pg impact winter[28], as sulfur-bearing gas would have resided in the stratosphere for a period of decades in the form of sulfate particles[8,28,29]. Previous studies[15,17] reported a longer cessation of solar irradiation as a result of stratospheric sulfate particles relative to the effect of dust particles, emphasizing the strong focus of previous modelling efforts on the role of sulfur release. Since the mid-1980s, a soot-driven K-Pg impact winter has also been postulated[20]. The impact-generated soot particles could also have played a dominant role in the global blockage of solar irradiance and the prolonged post-impact cooling[30], as fine soot constitutes a strong sunlight absorber[18,22,23]. Soot and charcoal remains found in the K-Pg boundary intervals around the world suggest widespread wildfires in the aftermath of the Chicxulub impact[20]. These wildfires were probably formed proximally during the first 'fireball stage' and potentially also elsewhere around the globe due to the thermal radiation from the atmospheric re-entry of hypervelocity ejecta[31-34]. A recent molecular-burn marker study revealed that up to 17% of the soot release was derived directly from Yucatán target rock, while the remainder was sourced from delayed wildfires[35]. However, the overall extent and intensity of these wildfires are still debated[10].

The third type of fine-grained ejecta represents the silicate dust, which remains a poorly understood group mainly because of a limited number of studies measuring their particle-size distribution. This dust is clearly finer than other silicate ejecta such as coarse glassy impact spherules (microtektite-like; with diameters ranging from ~300 µm to 2 mm (ref. 36)) and ejected mineral clasts (for example, shocked quartz, zircon, feldspar; diameters ranging from ~30 to 600 µm (refs. 9,37)), both of which are associated with ejecta curtain processes[10] (Fig. 1a,b), as well as crystalline impact spherules (microkrystites with, for example, Ni-rich spinels; diameters ranging from ~100 to 300 µm (refs. 36,38)), which are linked to condensation out of the vapour-rich impact plume[36,38] (Fig. 1c,d). Previous studies considered two subgroups of silicate K-Pg dust[39]. The first subgroup consists of material with a median diameter of 0.5 µm (ref. 39) and is known as submicron clastic dust. However, the amount of this subgroup was estimated to be <6 × 10^16 g and was therefore considered less important to the post-impact climate change[27,39]. The other subgroup represents nanoparticles, potentially iron-rich[40], with a median diameter of 20 nm (ref. 39). Their total mass was estimated to be much larger, at 2 × 10^18 g (ref. 39) as an upper limit, and recent climate model results using ballistic ejection of this subgroup led to their rapid atmospheric removal within nearly 2 yr after impact[18].

To understand the K-Pg dust conundrum, this study includes high-resolution sedimentological constraints from an expanded and well-preserved K-Pg sequence from the US western interior (Tanis, North Dakota; Fig. 1b,d and Extended Data Fig. 1). In contrast to other intermediate or distal K-Pg boundary sites, in which the K-Pg clay interval is around 1 cm thick and different types of impact ejecta are often mixed, the unique Tanis K-Pg record is expanded and allows for subselection of specific time frames during the Chicxulub impact ejecta deposition. The ~1.3-m-thick ejecta-bearing sediment package emplaced by a Chicxulub impact-generated tsunami-like surge (Fig. 1b and Extended Data Fig. 1) was deposited exclusively during the period of coarse ejecta accretion, probably corresponding to <2 h post-impact[41]. Shocked quartz grains have been found only in the un-reworked K-Pg claystone that conformably overlies the impact
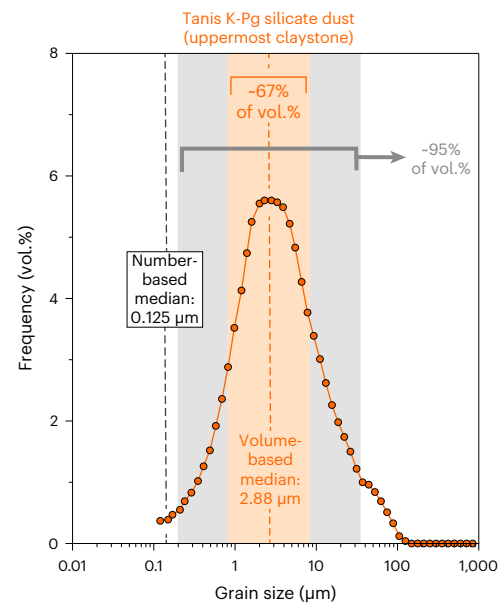

Fig. 2 | Volume-weighted K-Pg boundary grain-size data. The laser-diffraction grain-size distribution curve is shown of the silicate lithogenic fraction for the uppermost K-Pg boundary claystone level from the Tanis site, just below the Palaeocene lignite (see Extended Data Fig. 1 for a detailed stratigraphy). The orange curve displays the volume-based grain-size distribution, with the orange bar and blue representing ~67 and ~95% of the data, respectively (corresponding to grain-size ranges of ~0.8–8.0 µm and ~0.2–35.0 µm, respectively). The black dashed line highlights the median grain-size value after a conversion into a number density spectrum (see Methods and Extended Data Fig. 2 for the converted number density spectrum).

spherule-bearing Tanis deposit (Fig. 1b,d). On the basis of ballistic trajectory simulations, these shocked minerals are expected to arrive at Tanis in ~2 h after impact[9], corroborating the temporal control. A positive iridium anomaly exists in this K-Pg claystone (3.8 ppb (ref. 41)), which is linked to impactor material and is comparable in concentration to other globally distributed K-Pg localities[6]. The uppermost part of the K-Pg claystone interval, just below the Palaeogene lignite, is considered representative of the final atmospheric settling of the fine silicate dust, rich in iridium (Fig. 1d). Laser-diffraction grain-size analysis performed on the different strata at the Tanis K-Pg site quantifies the particle-size distributions (Methods and Extended Data Fig. 1). This uppermost K-Pg claystone interval represents a distinct, uniform and very fine distribution with a volume-based median grain size of 2.88 µm (Fig. 2), and after converting to a number density spectrum with a median grain size of 0.125 µm (mass to number density spectrum conversion in Methods; Extended Data Fig. 2). These size distribution data are used here as an input parameter to simulate the silicate dust scenario.

Previous atmospheric modelling studies investigating the radiative effect of silicate dust following the Chicxulub impact event[18,39] have used either nanometric-sized particles or coarse impact spherule data as the bulk fraction of silicate dust injection, both of which are estimated to be on the order of 2 × 10^18 g as an upper limit. The dominant grain sizes between ~0.8 and 8.0 µm measured at the Tanis K-Pg site result in substantially slower deposition than those used in previous palaeoclimate studies[18,39] (Fig. 3). In this Article, we incorporate this sedimentological data in our general circulation model (GCM)[19], which makes use of the latest Cretaceous palaeogeographic reconstructions[42] (Extended Data Fig. 1a) and the latest insights on the moment of impact, which is suggested to be the boreal spring season on the basis of recent data from the Tanis K-Pg site[38] (Methods). In our palaeoclimate GCM simulations (see Methods for details), we injected into the atmosphere the same amount of silicate dust (2 × 10^18 g (ref. 39)), fine soot
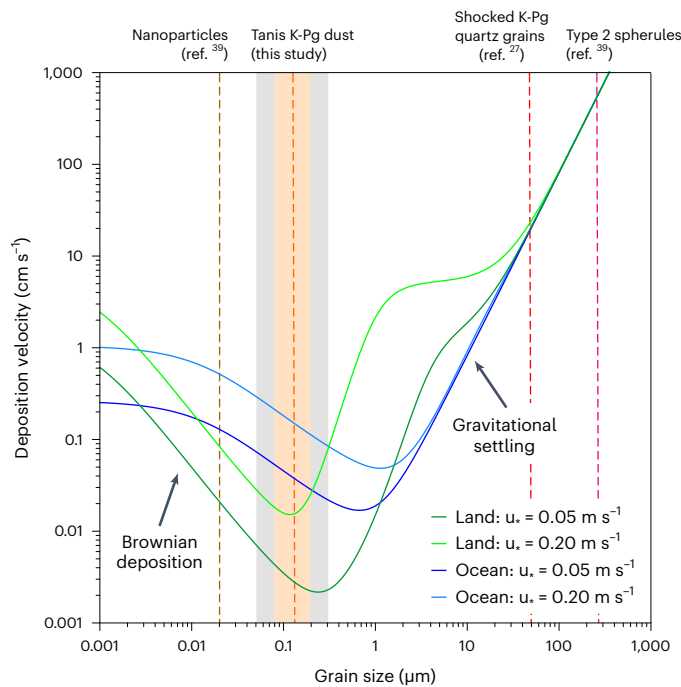
Fig. 3 | Number-weighted K-Pg boundary grain-size data in relation to atmospheric settling processes. Phase diagram shows grain size versus the variation of dry deposition velocity over land (green solid curves) and ocean (blue solid curves) for two typical friction velocity values, u_*, on Earth, indicating the intensity of surface wind shear (Methods). The nonlinear responses of deposition rates along with particle sizes are controlled by the relative contributions of gravitational and aerodynamic forcing, besides the Brownian diffusion, impaction and interception of particles (Methods). Previous modelling studies[18,39] have used three groups of ejected dust in different sizes. The first group is nanometric in size (median of 0.02 μm; brown dashed line), following a fast Brownian deposition. The second group comprises ejected (shocked) quartz grains (defined by ref. 27 as clastic debris; red dashed line) with a mean size of 50 μm (ref. 37). Together with the third group, the type 2 spherules (microkrystites[39]) with a median size of 250 μm (purple dashed line), this follows a fast gravitational settling. These literature data contrast the silicate dust fraction measured at the Tanis K-Pg site (number-based median of 0.125 μm with two-thirds of the particles by number density falling in the range of ~0.08–0.19 μm and 95% of the data falling in the range of ~0.05–0.30 μm; orange and blue dashed line and bar). This implies a considerably slower deposition for the impact-generated dust, by a factor of ~3–4 compared with the nanoparticles and by a factor of ~10 or at least 100 compared with the ejected quartz grains and type 2 spherules, respectively.

(2.08×10^{16} g (ref. 18), using a median diameter of 0.22 μm (ref. 39); Extended Data Fig. 3) and sulfur (3.25×10^{17} g (ref. 16), equivalent to 6.5×10^{17} g SO_2 (ref. 18)) as used in recent K-Pg modelling studies to directly compare the simulation results from our dust model with previous works[10,16,18,39]. Using these input parameters, the individual scenarios are modelled for silicate dust, soot and sulfur, accompanied by a combined scenario. In this Article, we carefully document the short-term global environmental consequences of the Chicxulub impact with a focus on changes in the photosynthetic active radiation (PAR; Methods). This solar radiation from 400 to 700 nm is being used by organisms in the process of photosynthesis and therefore represents an efficient indication for the state of the biosphere.

Cooling in the aftermath of the Chicxulub impact

Our palaeoclimate simulations show global temperatures changing seasonally between ~15 and 19 °C before the impact event, in line with proxy-based latest Cretaceous temperature reconstructions[43–45], despite a larger meridional temperature gradient compared with the proxy temperatures (Extended Data Fig. 4). The K-Pg impact winter catastrophically disrupted this greenhouse climate, leading to plummeting temperatures in both the marine and especially the terrestrial realm (Extended Data Fig. 5). The global-average surface temperature dropped by as much as 25 °C (Fig. 4a). With varying magnitude and timescales, each fine-grained ejecta type results in a prolonged global cooling in the initial aftermath of the impact. The sulfur scenario causes the lowest surface temperatures, with a global average of –3 °C, followed by the silicate dust scenario, with a global average of ~7 °C. Our simulations indicate that both sulfur and silicate dust have a prominent influence on the surface thermal forcing, leading to a prolonged impact winter up to ~20 yr, in which the first 5–8 yr are the most severe.

Relative radiative contributions of dust, sulfur and soot

The ejecta type and its atmospheric mass determines the magnitude and timescale of the impact winter (Fig. 4b), related to different responses in net short-wave/long-wave radiation (Extended Data Fig. 6 and Methods) and downward long-wave radiation (Fig. 4c) on the surface. The latter indicates the reflected infrared radiation due to atmospheric particles and clouds, which may either diminish or further enhance surface warming. Indeed, it plays a crucial role in Earth's climate as a vital factor controlling surface warming. The mass of sulfate particles in the atmosphere decreases much faster than dust, such that the global column-integrated mass of sulfur is reduced to about two orders of magnitude lower than that of dust at 3 yr after impact (Fig. 4b). Because of the radiatively transparent optical feature of sulfate particles[39], the sulfur emission is not able to enhance the downward long-wave radiation. In just a few years (Fig. 4c), it drops by 31.4% from its pre-impact level, thus allowing more long-wave radiation and causing the most cooling of all the impact scenarios (Fig. 4a). The decline or enhancement of the downward long-wave radiation is what makes the distinction between sulfur and dust cases, respectively, linked to the differences in particle optical properties, that is, specific extinction, single-scattering albedo and asymmetry factor (Methods). The dust-induced downward long-wave radiation shows a rapid increase by 64.4% from the pre-impact level to 372 W m^{-2} in a week after impact (Fig. 4c), leading to relatively warm surface temperatures more than ~10 °C compared with the sulfur case (Fig. 4a). Following the initial 3 yr after impact, the downward long-wave radiation increases gradually to the pre-impact level (210 W m^{-2}), lasting below pre-impact level ~20 yr in all cases except the soot-only case, which reached the pre-impact level in ~8 yr (Fig. 4c). This trend is consistent with the gradual global warming pattern at the same time frame (Fig. 4a). Our simulation results depict that the radiative feedback of the combined emissions scenario (Fig. 4c,d and Extended Data Fig. 6), hence the surface cooling (Fig. 4a), does not result in the sum of individual ejecta groups but rather falls between sulfur and dust cases associated with distinct radiation responses. It is governed largely by nonlinear interaction processes in the atmosphere, such as the complex dynamics of aerosol transport and deposition mechanisms interacting with turbulent atmospheric circulations and the water cycle.

Photosynthetic active radiation cessation following impact

The global-average PAR (Methods) flux in the sunlight spectrum varies seasonally between 80 and 95 W m^{-2} in the latest Cretaceous period (Fig. 4d). The global mean corresponds to 89 W m^{-2}, which is larger than the present-day global PAR flux (66–74 W m^{-2}; Methods). Because of the seasonality, the PAR flux is as high as 160 W m^{-2} in the Northern Hemisphere just before the impact winter (Extended Data Fig. 7 and Methods). The first-day response (Fig. 5) displays the trace of initial ejecta expansion through the atmosphere, marking a regional PAR deficit on the surface. Given that the dust and sulfur are ejected from the impact target, their traces are initially centralized around the Yucatán
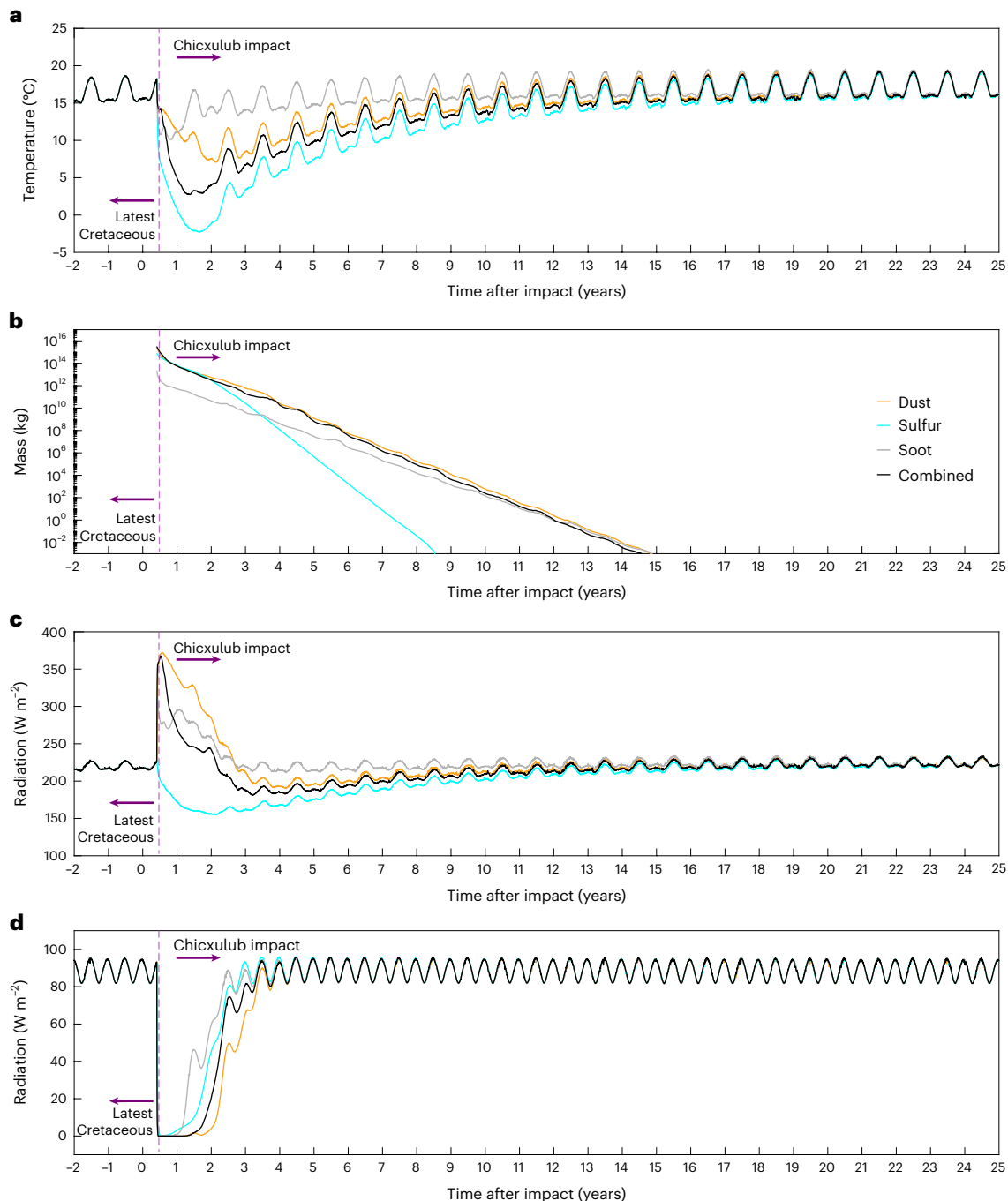
Fig. 4 | Temporal evolution of the Chicxulub impact-generated global climatic responses. The time evolution is shown from 2 yr of the latest Cretaceous towards 25 yr of post-impact conditions, for the individual silicate dust, sulfur, soot and combined scenarios. **a**, Global-average surface temperature. **b**, Global column-integrated fine-grained ejecta mass.

c, Global-average surface downward long-wave radiation flux. **d**, Global-average PAR flux. On the *x* axis, the year 0 refers to the start of the year when the impact event occurs. The solid purple dashed line denotes the moment of Chicxulub impact, that is, during the boreal spring season[38].

area, unlike the global spread of soot released from wildfires (Methods). Within two weeks after impact, the planet undergoes a global shut-down in photosynthetic activity in all ejecta scenarios (Extended Data Fig. 8). Consistent with global-average responses (Fig. 4d), the massive dust ejecta indicates the largest influence on the land–ocean photosynthetic activity, leading to an entire PAR suppression for ~1.7 yr (Fig. 5a). Even 2.2 yr after impact, during boreal summer, the photosynthetic activity remains low although in partial recovery with a moderate PAR flux of 100 W m^{-2} (Fig. 5a), reaching pre-impact values in ~4 yr after impact

(Fig. 4d). Following the initial suppression of six months (Fig. 4d), the PAR deprivation in sulfur and soot cases recovers faster (>1 yr) than in the dust case (Fig. 5a,b,c). This relatively rapid PAR recovery clearly documents that, alone, these two factors (sulfur and soot) are much less lethal than dust. Moreover, the combined emissions scenario indicates a global PAR cessation even at ~1.7 yr after impact (Fig. 5d). It fully recovers only after ~4 yr after impact, similar to the dust scenario (Fig. 4d), implying that the dust is the most lethal for the planet's photosynthetic cessation.
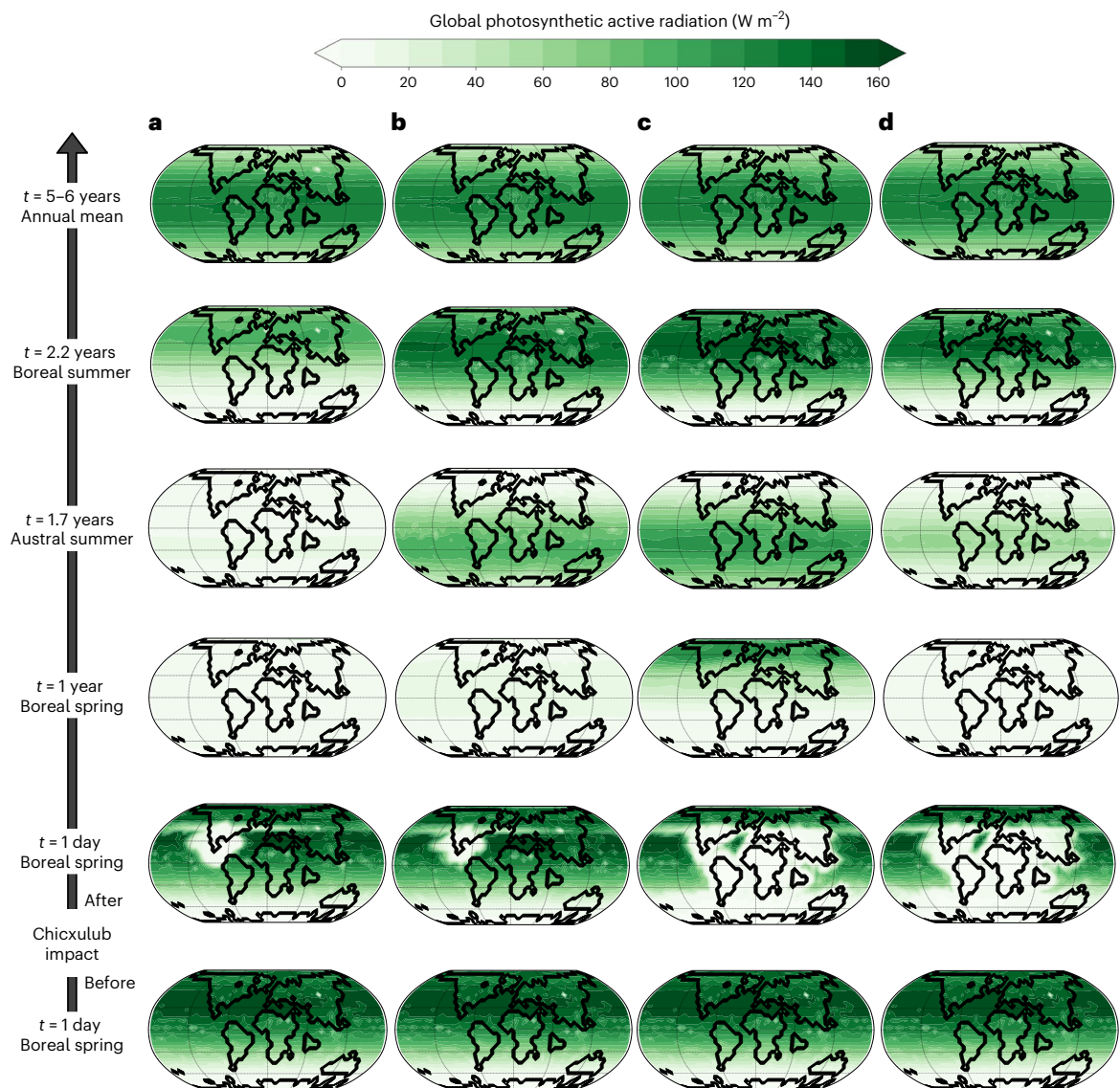
Fig. 5 | Temporal evolution of PAR flux reconstructions after the Chicxulub impact. a–d, Land and ocean PAR flux from one day before (pre-impact state) and after (post-impact state) in Boreal spring instantaneously towards 5–6 yr (annual mean) in the aftermath of the Chicxulub impact for silicate dust (**a**), sulfur (**b**), soot (**c**) and combined (**d**) scenarios, displayed on a latest Cretaceous palaeogeographic map (Extended Data Fig. 1a). The range of the green–white colour bar represents the photosynthetically high and low radiative flux. Basemaps are based on the latest Cretaceous palaeogeographic data for the latest Cretaceous[42].

Implications for the K-Pg climate and biota

In contrast to previous work[8,18,22,26], our palaeoclimate simulations, relying on robust sedimentological field data at the K-Pg, revealed that a massive impact-generated dust plume plays a large part in driving the K-Pg climate and biotic crisis. This dust cloud is composed of a large number of climate-active particles with grain sizes primarily in the range of 0.8–8.0 μm by volume (Fig. 2). This information is deciphered from laser-diffraction grain-size analysis from the uppermost K-Pg boundary claystone of the terrestrial Tanis site (median of 2.88 μm), which shows a comparable grain-size distribution as the deep marine ODP 1212 site in the Pacific Ocean (2–4 μm (ref. 46)). Our palaeoclimate simulations indicate that this micrometric grain-size pattern results in an atmospheric residence time that is much longer (>2 times) compared with previously estimated nano-sized or coarse particles[18,27,39] (Fig. 3 and Extended Data Fig. 9). Among simulated ejecta types, our simulations demonstrate a post-impact world where the silicate dust represents the largest ejected mass in the initial aftermath of impact (Fig. 4b). The sulfur scenario exhibits the fastest deposition with an

atmospheric lifetime of only ~8.5 yr. By contrast, both soot and silicate dust resided in the atmosphere considerably longer, for ~15 yr after impact. Similarly, the combined emissions scenario shows an atmospheric lifetime of ~15 yr, implying a plausible condition for the Chicxulub impact. The complete recovery from the impact winter took even longer, with pre-impact temperature conditions returning only after ~20 yr (Fig. 4a and Extended Data Fig. 10). This timescale is consistent with the recent global iridium layer observations[6] from the Chicxulub impact structure, where the final atmospheric settling of fine-grained impactor material in the dust cloud was estimated to be <20 yr.

We find that the global darkness and prolonged loss in the planet's photosynthetic activity occur only in the silicate dust scenario, up to nearly 1.7 yr (620 days) after impact (Figs. 4d and 5a–c). This constitutes a sufficiently long timescale to pose severe challenges for both terrestrial and marine habitats. Biotic groups that were not adapted to survive the dark, cold and food-deprived conditions for almost two years would have experienced massive extinctions. This matches the palaeontological records, which show that fauna and flora that could

enter a dormant phase (for example, through seeds, cysts or hibernation in burrows) and were able to adapt to a generalistic lifestyle, not dependent on one particular food source (for example, deposit feeders), generally better survived the K-Pg event[47]. In addition, our combined emissions scenario shows that the photosynthetic recovery to the pre-impact levels first occurred in the austral summer season, ~1.7 yr after impact. This would imply an earlier recovery of the primary productivity in the Southern Hemisphere, consistent with palaeontological evidence suggesting lower extinction levels on the Southern Hemisphere[48], resulting in geographic heterogeneity in extinction and recovery from the end-Cretaceous catastrophe. However, more high-resolution studies of K-Pg boundary records around the globe are needed to confirm the degree of hemispheric heterogeneity in the post-impact biotic recovery. To conclude, our results highlight that the photosynthetic shut-down induced by the large volume of silicate dust with grain sizes between ~0.8 and 8.0 μm, together with additional effects of sulfur and soot, probably led to a disastrous collapse of primary productivity in land and ocean realms, steering the global mass extinction at the K-Pg boundary.

Online content

Any methods, additional references, Nature Portfolio reporting summaries, source data, extended data, supplementary information, acknowledgements, peer review information; details of author contributions and competing interests; and statements of data and code availability are available at https://doi.org/10.1038/s41561-023-01290-4.

References

1. Smit, J. & Hertogen, J. An extraterrestrial event at the Cretaceous–Tertiary boundary. *Nature* **285**, 198–200 (1980).
2. Alvarez, L. W. et al. Extraterrestrial cause for the Cretaceous–Tertiary extinction. *Science* **208**, 1095–1108 (1980).
3. Kring, D. A. The Chicxulub impact event and its environmental consequences at the Cretaceous–Tertiary boundary. *Palaeogeogr. Palaeoclimatol. Palaeoecol.* **255**, 4–21 (2007).
4. Schulte, P. et al. The Chicxulub asteroid impact and mass extinction at the Cretaceous–Paleogene boundary. *Science* **327**, 1214–1218 (2010).
5. Collins, G. S. et al. A steeply-inclined trajectory for the Chicxulub impact. *Nat. Commun.* **11**, 1480 (2020).
6. Goderis, S. et al. Globally distributed iridium layer preserved within the Chicxulub impact structure. *Sci. Adv.* **7**, eabe3647 (2021).
7. Chiarenza, A. A. et al. Asteroid impact, not volcanism, caused the end-Cretaceous dinosaur extinction. *Proc. Natl Acad. Sci. USA* **117**, 17084–17093 (2020).
8. Pierazzo, E., Kring, D. A. & Melosh, H. J. Hydrocode simulation of the Chicxulub impact event and the production of climatically active gases. *J. Geophys. Res. Planets* **103**, 28607–28625 (1998).
9. Alvarez, W., Claeys, P. & Kieffer, S. W. Emplacement of Cretaceous–Tertiary boundary shocked quartz from Chicxulub crater. *Science* **269**, 930–935 (1995).
10. Morgan, J. V. et al. The Chicxulub impact and its environmental consequences. *Nature Rev. Earth Environ.* **3**, 338–354 (2022).
11. Morgan, J. V. et al. The formation of peak rings in large impact craters. *Science* **354**, 878–882 (2016).
12. López-Ramos, E. in *Ocean Basins and Margins, the Gulf of Mexico and Caribbean* (eds Nairn, A. E. M. & Stehli, F. G.) 257–282 (Plenum Press, 1975).
13. Robertson, D. S. et al. K–Pg extinction patterns in marine and freshwater environments: the impact winter model. *J. Geophys. Res. Biogeosci.* **118**, 1006–1014 (2013).
14. Vellekoop, J. et al. Rapid short-term cooling following the Chicxulub impact at the Cretaceous–Paleogene boundary. *Proc. Natl Acad. Sci. USA* **111**, 7537–7541 (2014).
15. Brugger, J., Feulner, G. & Petri, S. Baby, it's cold outside: climate model simulations of the effects of the asteroid impact at the end of the Cretaceous. *Geophys. Res. Lett.* **44**, 419–427 (2017).
16. Artemieva, N., Morgan, J. & Party, E. S. Quantifying the release of climate-active gases by large meteorite impacts with a case study of Chicxulub. *Geophys. Res. Lett.* **44**, 10–180 (2017).
17. Brugger, J. et al. A pronounced spike in ocean productivity triggered by the Chicxulub impact. *Geophys. Res. Lett.* **48**, e2020GL092260 (2021).
18. Tabor, C. R. et al. Causes and climatic consequences of the impact winter at the Cretaceous–Paleogene boundary. *Geophys. Res. Lett.* **47**, e60121 (2020).
19. Senel, C. B. et al. Relative roles of impact-generated aerosols on photosynthetic activity following the Chicxulub asteroid impact. *GSA Connects* **53**, 6 (2021).
20. Wolbach, W. S., Lewis, R. S. & Anders, E. Cretaceous extinctions: evidence for wildfires and search for meteoritic material. *Science* **230**, 167–170 (1985).
21. Belcher, C. M. et al. Geochemical evidence for combustion of hydrocarbons during the KT impact event. *Proc. Natl Acad. Sci. USA* **106**, 4112–4117 (2009).
22. Kaiho, K. et al. Global climate change driven by soot at the K–Pg boundary as the cause of the mass extinction. *Sci. Rep.* **6**, 28427 (2016).
23. Bardeen, C. G. et al. On transient climate change at the Cretaceous–Paleogene boundary due to atmospheric soot injections. *Proc. Natl Acad. Sci. USA* **114**, E7415–E7424 (2017).
24. Sharpton, V. et al. in *Global Catastrophes in Earth History* (eds Virgil L. Sharpton, V. L. & Ward, P. D.) 349–357 (GSA, 1990).
25. Kaskes, P. et al. High-resolution chemostratigraphy of the Cretaceous-Paleogene (K-Pg) boundary interval in the US western interior: Implications for Chicxulub impact ejecta dynamics. In *53rd Lunar and Planetary Science Conference*, Vol. 2678, 2708 (2022).
26. Henehan, M. J. et al. Rapid ocean acidification and protracted Earth system recovery followed the end-Cretaceous Chicxulub impact. *Proc. Natl Acad. Sci. USA* **116**, 22500–22504 (2019).
27. Pope, K. O. Impact dust not the cause of the Cretaceous–Tertiary mass extinction. *Geology* **30**, 99–102 (2002).
28. Pope, K. O. et al. Impact winter and the Cretaceous/Tertiary extinctions: results of a Chicxulub asteroid impact model. *Earth Planet. Sci. Lett.* **128**, 719–725 (1994).
29. Pierazzo, E., Hahmann, A. N. & Sloan, L. C. Chicxulub and climate: radiative perturbations of impact-produced S-bearing gases. *Astrobiology* **3**, 99–118 (2003).
30. Wolbach, W. S. et al. in *Global Catastrophes in Earth History; An Interdisciplinary Conference on Impacts, Volcanism, and Mass Mortality* Vol. 247 (eds Sharpton, V. L. & Ward, P. D.) 219–220 (GSA, 1990).
31. Kring, D. A. & Durda, D. D. Trajectories and distribution of material ejected from the Chicxulub impact crater: implications for postimpact wildfires. *J. Geophys. Res. Planets* https://doi.org/10.1029/2001JE001532 (2002).
32. Morgan, J., Artemieva, N. & Goldin, T. Revisiting wildfires at the K–Pg boundary. *J. Geophys. Res. Biogeosci.* **118**, 1508–1520 (2013).
33. Goldin, T. J. & Melosh, H. J. Self-shielding of thermal radiation by Chicxulub impact ejecta: firestorm or fizzle? *Geology* **37**, 1135–1138 (2009).
34. Harvey, M. C. et al. Combustion of fossil organic matter at the Cretaceous–Paleogene (KP) boundary. *Geology* **36**, 355–358 (2008).
35. Lyons, S. L. et al. Organic matter from the Chicxulub crater exacerbated the K–Pg impact winter. *Proc. Natl Acad. Sci. USA* **117**, 25327–25334 (2020).

36. Smit, J. The global stratigraphy of the Cretaceous–Tertiary boundary impact ejecta. *Annu. Rev. Earth Planet. Sci.* **27**, 75–113 (1999).

37. Bostwick, J. A. & Kyte, F. T. in *The Cretaceous–Tertiary Event and Other Catastrophes in Earth History* (eds Ryder, G., Fastovsky, D. E. & Gartner, S.) 403–415 (GSA, 1996).

38. During, M. A. D. et al. The Mesozoic terminated in boreal spring. *Nature* **603**, 91–94 (2022).

39. Toon, O. B., Bardeen, C. & Garcia, R. Designing global climate and atmospheric chemistry simulations for 1 and 10 km diameter asteroid impacts using the properties of ejecta from the K–Pg impact. *Atmos. Chem. Phys.* **16**, 13185–13212 (2016).

40. Belza, J. et al. Petrography and geochemistry of distal spherules from the K–Pg boundary in the Umbria–Marche region (Italy) and their origin as fractional condensates and melts in the Chicxulub impact plume. *Geochim. Cosmochim. Acta* **202**, 231–263 (2017).

41. DePalma, R. A. et al. A seismically induced onshore surge deposit at the KPg boundary, North Dakota. *Proc. Natl Acad. Sci. USA* **116**, 8190–8199 (2019).

42. Markwick, P. J. & Valdes, P. J. Palaeo-digital elevation models for use as boundary conditions in coupled ocean–atmosphere GCM experiments: a Maastrichtian (late Cretaceous) example. *Palaeogeogr. Palaeoclimatol. Palaeoecol.* **213**, 37–63 (2004).

43. Upchurch, G. R. et al. Latitudinal temperature gradients and high-latitude temperatures during the latest Cretaceous: congruence of geologic data and climate models. *Geology* **43**, 683–686 (2015).

44. O'Brien, C. L. et al. Cretaceous sea-surface temperature evolution: constraints from TEX86 and planktonic foraminiferal oxygen isotopes. *Earth Sci. Rev.* **172**, 224–247 (2017).

45. Niezgodzki, I. et al. Late Cretaceous climate simulations with different CO_2 levels and subarctic gateway configurations: a model–data comparison. *Paleoceanography* **32**, 980–998 (2017).

46. Bralower, T. et al. Grain size of Cretaceous–Paleogene boundary sediments from Chicxulub to the open ocean: implications for interpretation of the mass extinction event. *Geology* **38**, 199–202 (2010).

47. Vellekoop, J. et al. Type-Maastrichtian gastropod faunas show rapid ecosystem recovery following the Cretaceous–Palaeogene boundary catastrophe. *Palaeontology* **63**, 349–367 (2020).

48. Donovan, M. P. et al. Rapid recovery of Patagonian plant–insect associations after the end-Cretaceous extinction. *Nat. Ecol. Evol.* **1**, 0012 (2016).

49. Belza, J. *Petrography and geochemistry of ejecta material from the K-Pg boundary Chicxulub crater (Yucatan, Mexico)*. PhD thesis, Vrije Universiteit Brussel (2015).

50. Pierazzo, E. & Artemieva, N. Local and global environmental effects of impacts on Earth. *Elements* **8**, 55–60 (2012).

Methods

Laser-diffraction grain-size analysis of K-Pg boundary sediments

Laser-diffraction grain-size analysis was performed on 40 sediment samples from the X-2741-A and X-2761 (Supplementary Table 1) sections from the Tanis K-Pg site (North Dakota, United States[41]) to decipher the depositional processes of the Upper Cretaceous point bar strata, unit K, the event deposit, units 1 and 2, as well as the Palaeocene intervals, P1 and P3 (Extended Data Fig. 1b). The analysis took place at the Sediment Laboratory at the Vrije Universiteit Amsterdam using a Sympatec HELOS KR laser-diffraction particle-size analyser[51]. Before particle-size analysis, the sediment samples were prepared following a procedure[52] to ensure solely the lithogenic fraction was measured. Organic matter and carbonate material were removed by treating the samples with 5–10 ml 30% H_2O_2 and 5–10 ml 10% HCl, respectively, both followed by heating to boiling point. After decarbonization, the Palaeocene lignite samples (unit P2) did not yield sufficient lithogenic fraction to achieve accurate results. To prevent clumping of clay minerals to agglomerates, 300 mg sodium pyrophosphate ($Na_4P_2O_7 \cdot 10H_2O$) was added to the suspension, followed again by heating until boiling point. After cooling, the samples in suspension were measured in the HELOS laser-diffraction sensor device, with the resulting lithogenic grain-size distribution data (ranging from 0.1 to 2,000 μm, measured in 56 classes) expressed in volumetric percentage.

A clear two-step fining upward sequence is recognized in the Tanis K-Pg boundary succession (Extended Data Fig. 1b), which has been attributed to the arrival of two successive tsunami-like surge waves generated by the Chicxulub impact event[41]. The sample just below the Palaeocene lignite, together with the other two K-Pg claystone samples, reveals a distinct and uniform particle-size distribution with ~80% clay fraction, indicative of fine atmospheric settling[53]. This sharply contrasts with the Tanis event deposit, which shows large heterogeneities with more pronounced bimodal distributions, including a coarser peak of fine sand around 125 μm, indicative of transport by water[51] (Extended Data Fig. 1c). The uppermost K-Pg claystone sample yields a very fine median of 2.88 μm (Fig. 2a and Extended Data Fig. 1c), and this grain-size distribution was used in our numerical modelling study. Note that the measured mass density spectrum is fitted by a trimodal log-normal size distribution (see the model parameters of each mode; Extended Data Fig. 2a).

Mass to number density spectrum conversion

This analysis transforms the mass density spectrum of K-Pg grain-size data into the number density spectrum (Extended Data Fig. 2), which provides a compatible input for a GCM[54,55]. Let $Q_r(x_i)$ be a cumulative particle-size distribution from a given sediment sample:

$$\Delta Q_r(x_{i-1}, x_i) = Q_r(x_i) - Q_r(x_{i-1}) \tag{1}$$

In equation (1), x_i is the particle size and $\Delta Q_r(x_i)$ is a differential particle-size distribution. The spectrum density, $q_r(x_i)$, is given by:

$$q_r(x_i) = \frac{\Delta Q_r(x_i)}{\Delta x_i} = \frac{Q_r(x_i) - Q_r(x_{i-1})}{x_i - x_{i-1}} \tag{2}$$

Here r denotes the type of density spectrum: $r = 0$ (number) or $r = 3$ (mass). To convert $q_r(x_i)$ from $r = 3$ to $r = 0$, we followed a well-described method[56]. First, a given density spectrum $q_e(x_i)$ can be transformed into $q_r(x_i)$ by:

$$q_r(x_i) = x_i^{r-e} q_e(x_i) / \mathcal{M}_{r-e,e} \tag{3}$$

In equation (3), $\mathcal{M}_{r-e,e}$ is the moment of distribution. The moment of particle-size distribution can be generalized by:

$$\mathcal{M}_{k,r} = \int_{x_{i,\min}}^{x_{i,\max}} x_i^k q_r(x_i) \, dx_i = \frac{\mathcal{M}_{k+r-e,e}}{\mathcal{M}_{r-e,e}} \tag{4}$$

Here $\mathcal{M}_{k,r}$ is the kth moment of r-type density spectrum, $q_r(x_i)$. Since the transform will be applied from mass to number spectrum, recalling equation (3) and taking $e = 3$ and $r = 0$:

$$q_0(x_i) = x_i^{-3} q_3(x_i) / \mathcal{M}_{-3,3} \tag{5}$$

Supposing a log-normal particle-size distribution, the kth moment of a spectrum density, $q_r(x_i)$, can be expressed as follows:

$$\mathcal{M}_{k,r} = x_{g,r}^k \exp\left(\frac{k^2}{2} \ln^2 \sigma_{g,r}\right) \tag{6}$$

In equation (6), w_g and σ_g denote the median and standard deviation of particle-size distribution, respectively. Substituting $k = -3$ and $r = 3$ into equation (6), we have the following expression:

$$\mathcal{M}_{-3,3} = x_{g,3}^{-3} \exp\left(\frac{(-3)^2}{2} \ln^2 \sigma_{g,3}\right) = x_{g,3}^{-3} \exp\left(4.5 \ln^2 \sigma_{g,3}\right) \tag{7}$$

Then substituting equation (7) into equation (5), the final form of transformation is as follows:

$$q_0(x_i) = x_i^{-3} \frac{q_3(x_i)}{x_{g,3}^{-3} \exp\left(4.5\ln^2 \sigma_{g,3}\right)} \tag{8}$$

In equation (8), $q_3(x_i)$ is the mass density spectrum and $q_0(x_i)$ is the number density spectrum.

Modelling the log-normal number density spectrum

This was carried out by using the output of laser-diffraction analysis, $q_3^*(x_i)$, referring to the mass density spectrum on the logarithmic abscissa (Extended Data Fig. 2a). Here, $q_3^*(x_i)$ is defined by the logarithm of base 10 that can be expressed as:

$$\bar{n}_q^\circ(\log x_i) = q_3^*(x_i) \tag{9}$$

By converting equation (9) into the natural logarithm:

$$\bar{n}_q^e(\ln x_i)\, d\ln x_i = \bar{n}_q^\circ(\log x_i)\, d\log x_i \rightarrow \bar{n}_q^e(\ln x_i) = \bar{n}_q^\circ(\log x_i)/2.303 \tag{10}$$

Letting $D_p = x_i$ is more convenient to denote the particle size. Then $\bar{n}_q^e(\ln D_p)$, the mass density spectrum, can be transformed to number density spectrum, $\bar{n}_N^e(\ln D_p)$; by substituting into equation (8), we have following:

$$\bar{n}_N^e(\ln D_p) = D_p^{-3} \frac{\bar{n}_q^e(\ln D_p)}{D_{pg,3}^{-3} \exp\left(4.5 \ln^2 \sigma_{g,3}\right)} \tag{11}$$

To satisfy a probability density function, equation (11) can be normalized by:

$$n_N^e(\ln D_p) = \frac{\bar{n}_N^e(\ln D_p)}{\displaystyle\int_{-\infty}^{\infty} \bar{n}_N^e(\ln D_p)\, d\ln D_p} \tag{12}$$

$\bar{n}_N^e(\ln D_p)$ The term can now be approximated by a log-normal probability density function.

$$n_N^e(\ln D_p) = \frac{dN_N^e}{d\ln D_p} = \frac{N}{\sqrt{2\pi}\ln\sigma_{g,0}} \exp\left(-\frac{(\ln D_p - \ln D_{pg,0})^2}{2\ln^2 \sigma_{g,0}}\right) \tag{13}$$

In equation (13), N refers to the number concentration of particle-size distribution. The exact expression needs to be given in the form of $n_N(D_p)$, instead of $\bar{n}_N^e(\ln D_p)$.

$$n_N^e(\ln D_p)\,\mathrm{d}\ln D_p = n_N(D_p)\,\mathrm{d}D_p \rightarrow n_N^e(\ln D_p) = n_N(D_p)\frac{\mathrm{d}D_p}{\mathrm{d}\ln D_p} = n_N(D_p)D_p \tag{14}$$

The term $n_N(D_p)$ in equation (14) reads as follows:

$$n_N(D_p) = \frac{n_N^e(\ln D_p)}{D_p} = \frac{N}{\sqrt{2\pi}D_p\ln\sigma_{g,0}}\exp\left(-\frac{(\ln D_p - \ln D_{pg,0})^2}{2\ln^2\sigma_{g,0}}\right) \tag{15}$$

Equation (15) can be rewritten in differential form.

$$n_N(D_p)\,\mathrm{d}D_p = \frac{1}{\sqrt{2\pi}D_p\ln\sigma_{g,0}}\exp\left(-\frac{(\ln D_p - \ln D_{pg,0})^2}{2\ln^2\sigma_{g,0}}\right) \tag{16}$$

To satisfy a log-normal probability density function, equation (16) is scaled by a weighting factor, ω_0.

$$n_N(D_p)\,\mathrm{d}D_p = \frac{\omega_0}{\sqrt{2\pi}D_p\ln\sigma_{g,0}}\exp\left(-\frac{(\ln D_p - \ln D_{pg,0})^2}{2\ln^2\sigma_{g,0}}\right) \tag{17}$$

Concisely, the procedure we followed is that the mass density spectrum from the laser-diffraction grain-size analysis, $q_3^*(x_i)$, is first converted to a number density spectrum via equation (11), which is in turn modelled through a log-normal probability density function using equation (17), to use as an input in GCM simulations. The model parameters in equation (17) were determined as follows (Extended Data Fig. 2b):

$$\omega_0 = 7.24, D_{pg,0} = 0.125\,\mu\text{m}, \ln\sigma_{g,0} = 0.446 \tag{18}$$

Here, $D_{pg,0}$ and $\ln\sigma_{g,0}$ are the median and logarithmic standard deviation of modelled number density spectrum, respectively.

GCM overview

We performed palaeoclimate GCM simulations by our paleoEarth implementation of the general-purpose planetWRF model[57]. The planetWRF model has been widely applied and validated for the modelling of planetary atmospheres[58–61] on the basis of the extensively used terrestrial atmospheric model, Weather, Research and Forecasting (WRF) model[62]. Here our paleoEarth model[19] is a GCM that is specialized to simulate the Chicxulub impact at the K-Pg boundary, using the latest Cretaceous palaeography for geographic boundary conditions[42]. Our GCM makes use of a simplified plant functional type scheme for land-surface conditions, approximating the latest Cretaceous vegetation[45]. It resolves the atmospheric transport of fine-grained ejecta (consisting of sulfur, soot and silicate dust) generated by the Chicxulub impactor, considering the radiative and microphysical feedback of climate-active ejections. Regarding the verification of GCM, the simulated pre-impact surface temperatures agree with proxy-based latest Cretaceous temperature reconstructions (Extended Data Fig. 4). Moreover, in a recent intercomparison study[10], our initial GCM reconstructions for the post-impact global temperature drop fall in line with those of previous GCM simulations following the Chicxulub impact. It is worth mentioning that our initial GCM[10] is further improved here. In the initial GCM[10], a simple algorithm is used for the dry deposition of tracers; however, in the present version, we used an advanced atmospheric advection scheme of tracers available in the planetWRF. We updated the optical properties of soot and dust, such as the specific

extinction, single-scattering albedo and asymmetry factor as a function of wavelengths, which led to less surface cooling with regard to the climatic response of dust and soot emissions. Moreover, soot particles were injected only from the impact site, up to the stratosphere top in our initial GCM[10], which we updated here in the present version injecting soot only over the land surfaces from the surface up to lower stratosphere ('Emission configurations'). Note that we added an algorithm into the present GCM that conserves the global mass of emitted tracers (sulfur, soot, or dust) over the whole GCM domain from one time step to the next one. Consequently, the global mass of tracers is precisely conserved in the atmosphere, sustaining monotonic tracer deposition. The paleoEarth GCM consists of three main components besides the dynamical core of planetWRF. The first component is a module implemented for the asteroid/cometary impact dynamics, in which the transport of impact-generated fine-grained ejecta (consisting of sulfur, soot and silicate dust) is governed in the GCM. The second and third components are radiative transfer and microphysics modules, respectively.

Radiative transfer and microphysics modelling

The radiative transfer module, the second component, is used to include the radiative effect of impact ejecta, such as the absorption, reflection and scattering by ejected particles in the short-wave and long-wave spectra. It was built within the NASA (National Aeronautics and Space Administration) Goddard short-wave/long-wave radiation scheme[63,64], that is, composed of eight spectral bands within the ultraviolet and visible range (<700 nm) and three spectral bands in the infrared region (>700 nm). In this component, specific extinction, single-scattering albedo and asymmetry factor of sulfate were set as functions of wavelengths in short-wave and long-wave spectral bands[65]. Regarding the dust, optical properties are specified following previous studies in the short-wave[66] and long-wave[67] spectrum. Optical properties of soot are determined in short-wave and long-wave spectral bands[68]. The microphysics module, the third component, resolves the microphysical processes of fine-grained ejecta, such as dry and wet deposition processes of soot, sulfur and silicate dust. Microphysical processes are crucial in determining deposition rates and, as a result, the lifetimes of deposited particles in the atmosphere. For the dry deposition modelling of soot and dust, our GCM considers relative contributions of gravitational and aerodynamic forcing as well as the Brownian diffusion, impaction and interception of particles, using a particle-size-aware resistance model[69–72].

$$V_d = V_g + (\mathcal{R}_a + \mathcal{R}_s + \mathcal{R}_a\mathcal{R}_sV_g)^{-1} \tag{19}$$

Here, V_d and V_g are the deposition and gravitational settling velocities, while $\mathcal{R}_a$ and $\mathcal{R}_s$ are aerodynamic and surface deposition resistances. The latter term reads as follows:

$$\mathcal{R}_s = \frac{1}{\epsilon_0 u_*(E_b + E_{im} + E_{in})} \tag{20}$$

In equation (20), $\varepsilon_0 = 3$ is an empirical constant[69] and u_* is the friction velocity of near-surface winds that the GCM computes. Here E_b, E_{im} and E_{in} are collection efficiencies related to Brownian diffusion, impaction and interception of particles determined from previous models[70–72]. The dry deposition rate of sulfate on land was set to 0.1 cm s^{-1}, referring to the value of coniferous and deciduous forest covering land[73]. Likewise, the ocean deposition rate is prescribed to be 0.1 cm s^{-1}, which falls between the 0.05 cm s^{-1} (ref. 73) and 0.20 cm s^{-1} (ref. 65) reported in previous studies. Note that our sulfur-cycle simulations do not include photochemistry reactions. We presumed that the sulfur injection is fully converted into sulfate as the maximum scenario ('Emission configurations') as sulfur has around three to four times higher deposition rates on land and in the ocean, 0.6–0.8 cm s^{-1}

(ref. [65]), leading to faster deposition than sulfate. Moreover, the wet deposition of particles is modelled by resolving in-cloud rainout and washout processes[74–76]. For the dust microphysical modelling, our GCM takes dust lifting into account, consisting mainly of three mechanisms: (1) dust lifting by aerodynamic forces, (2) saltation bombardment and (3) breakdown of large aggregates (disaggregation)[77,78]. Note that the microphysical modelling of soot and dust were implemented in a size-resolved way[69] unlike the monodisperse assumption in sulfate modelling. Here the size-resolved modelling follows both our recent two-moment dust transport scheme initially derived for the Martian dust cycle[61] and a two-moment framework widely used in community atmosphere models[69]. Our soot and dust microphysics models do not include coagulation microphysics, which might pose as important for the transport of aerosols in the atmosphere. Nanometric particles below 0.1 μm, that is, 0.015 μm $< D_p <$ 0.052 μm, whose range is referred to as the Aitken mode[79], are formed by two processes: (1) condensational growth on existing aerosol particles and (2) coagulation due to the random particle collisions. These nanometric particles can further grow into larger particles or chains, resulting in the so-called accumulation mode (0.056 μm $< D_p <$ 0.26 μm)[79], in which coagulation can still occur especially at high particle concentrations following the K-Pg impact. The median diameters of dust (0.125 μm) and soot (0.22 μm) in our simulations are larger than the Aitken-mode interval while lying within the range of accumulation mode (Extended Data Fig. 3). In our GCM, the inclusion of a coagulation scheme would have formed larger soot aggregates up to 0.26 μm (the upper range of accumulation mode). Ref. [23] put forward that the coagulation can increase short-wave optical properties owing to the large soot emissions. Such particle sizes (up to 0.26 μm) are close to the median diameter of soot (0.22 μm), falling well into the high-probability range of log-normal size distribution used in our size-aware two-moment aerosol scheme. Therefore, any alteration in particle deposition and atmospheric lifetime or radiative response would be minor. This may also apply to the dust case. Even if larger dust aggregates with the same upper range (up to 0.26 μm) would form by the coagulation, the median size of dust particles (0.125 μm) would be close to the given size range. Despite a slight underestimation in current radiative response, such a change in particle size up to 0.26 μm would not have substantial influence on the atmospheric settling processes on land and ocean (Fig. 4) and thus on our main findings. Therefore, we assume the effect of coagulation to be lesser on the overall atmospheric processes of the given soot and silicate dust ejecta following the Chicxulub impact.

Description of simulation set-up and model physics

For the land-surface physics, in our GCM simulations we made use of the five-layer thermal diffusion scheme[80]. To model the water-cycle, cloud and precipitation microphysics, we used the Purdue–Lin microphysics scheme[81]. The modified Tiedtke scheme is utilized for the cumulus parameterization[82,83]. The planetary boundary-layer turbulence is modelled by means of our recent planetary boundary-layer scheme[84]. The atmospheric surface layer is modelled by using the revised MM5 scheme[85]. Regarding ocean modelling, we use the Pollard ocean mixed layer model[86,87] that accounts for the wind-driven turbulent mixing and deepening in the ocean. As we are interested mainly in the relative roles of different aerosols, we do not expect that using a more-sophisticated ocean and/or land surface would change our main conclusions. Moreover, we imposed the latest Cretaceous climatic conditions, taking global-average atmospheric CO_2 concentration to be 560 parts per million[15,18]. In our GCM simulations, we did not release CO_2 due to impact heating and global wildfires. It has no dominant effects on short timescales as focused in the present study, leading to a long-term warming of about 100,000 years since the impact winter[10]. Although it could induce global warming shortly after the K-Pg impact, the extent of warming is minor. Simulations[10,17] indicate that the change of C release from 115 to 1,615 Gt can result in ~2 °C warming from 5 to

20 years after impact. For the orbital forcing, a circular orbit with an obliquity of 23.5° and a solar constant of ~1,354 W m^{-2} are assumed[15], similar to other palaeoclimate studies[18,45]. The moment of the Chicxulub impact, thus the release of fine-grained ejecta, is assumed to be initialized in the boreal spring[38]. This assumption is based on recent osteohistological and isotopic studies from uniquely preserved fossil fish from the Tanis K-Pg site, and this moment of impact probably substantially influenced selective biotic survival across the K-Pg boundary catastrophe[38]. The horizontal model resolution of GCM is 5° × 5° over longitudinal and latitudinal directions, having 27 vertical sigma layers extending through the stratopause. Furthermore, the time integration for each impact simulation is carried out for 35 years following an initial spin-up simulation of 15 years, in which the latest Cretaceous conditions stabilized (Extended Data Fig. 10).

Calculation of PAR flux

PAR flux refers to the solar radiation reaching the surface in the λ = 400–700 nm spectral range, indicating how intense the radiative flux is to sustain photosynthesis being used by photosynthetic organisms[88]. It is thus highly important in quantifying the global primary production[89]. In our paleoEarth GCM, the time evolution of global PAR flux is computed within the radiative transfer module at each model time step. As the NASA Goddard short-wave/long-wave radiation scheme[63,64] solves the radiative transfer in spectral bands, the eighth spectral band corresponds to the PAR spectral range, in which we saved model results at each hour and post-processed for detailed interpretations (Figs. 3d and 4). Our simulations show that the global PAR flux is 89 W m^{-2} in the latest Cretaceous, which is larger than the present-day fluxes (66–74 W m^{-2}). Here we computed the present-day range following the approach[90] in which the PAR flux is converted as the fraction ($k_t \approx$ 0.45–0.5) of global solar irradiance reaching Earth's surface (R_s). The annual mean of global-average R_s was taken to be 147.3 W m^{-2} from the ten-year radiation budget of Earth between 1984 and 1993 (ref. [91]).

Emission configurations

The particles were emitted instantaneously at the moment of impact. In our GCM, the latest Cretaceous conditions stabilize following an initial spin-up simulation of 15 years. The next year (t = 16 yr) hosts the impact event when the day of year is 151, falling into the boreal spring season[38]. Ref. [10] reported that the fast-moving ejecta cloud could carry dust, soot and sulfate particles across Earth within four to five hours of impact. Silicate dust and sulfur spread are slower due to atmospheric transport; nevertheless, our GCM results show almost a global coverage already at one day after impact (Fig. 5). Here we injected sulfur and silicate dust from the impact site uniformly in the atmospheric column and up to the model top, that is, top of the stratosphere, while soot particles were injected over the whole land surfaces following ref. [18]. The current emissions design of silicate dust and sulfur may affect aerosol concentrations within the first few days after impact (up to the first week), overestimating concentrations near the impact site compared with distant locations. Enormous quantities of sulfur (~325 Gt) and silicate dust (~2,000 Gt) travelling at hypervelocities exceeding 5 km s^{-1} (ref. [10]) could suggest that the silicate dust and sulfur can rather be ejected globally as in ref. [39]. Nevertheless, emitting from the impact site instead of injecting globally would not have a notable influence on the timescale focused in our study (from first few weeks to 25 years). Concerning the emissions design of soot, for the vertical distribution, ref. [39] suggested a Gaussian vertical profile consisting of two peaks centred at the tropopause and surface. This way, the normalized injection rate at the surface (lower peak) is nearly three times larger than that at the tropopause (upper peak), in which the upper peak has a half width of 3 km injecting up to the altitude of 25 km. We injected soot particles from the surface up to 25 km (lower stratosphere), while assuming a uniform profile. Our approach is based on the assumption that the rapidly moving ejecta cloud, comprising large quantities of

soot (~20.8 Gt ref. [18])) from fires, disperse quickly in the vertical layers of atmosphere soon after impact. Strong vertical motions at high altitudes as well as up- and downdraughts, entrainment and turbulence in the boundary layer[39] could carry the smoke likely well mixed in troposphere and lower stratosphere. More-sophisticated injection profiles of soot as in ref. [39] could better estimate the atmospheric perturbations locally and vertically in the immediate aftermath of impact (first days to the first two weeks). However, it may have no substantial effect on the longer timescales, which we focused on in this study. Regarding the sulfur emission, given the relatively high rates of dry and wet deposition, therefore the reduced atmospheric lifetime of SO_2, we assumed that SO_2 is fully oxidized to form sulfate aerosols as the upper limit of atmospheric perturbations. The atmospheric lifetime of sulfate can be longer than our upper estimate as the conversion rate from SO_2 to sulfate may take a while[18] due to homogeneous or heterogeneous chemical pathways[92,93]. However, the water release from the shallow sea impact site[94] can speed up this conversion rate[95]. Moreover, a fraction of SO_2 can convert into more quickly removed SO_3 in the atmosphere, increasing the SO_3/SO_2 ratios within the impact vapour cloud. Impact experiments demonstrated that the major portion of sulfur in the impact ejecta occurs in the form of SO_3 (ref. [96]). If this is the case, it implies that the conversion to sulfate aerosols would form even more rapidly in the stratosphere[10]. Note that the vertical extent of our GCM spans from the planetary surface to the top of the stratopause. Here we focused on the relative roles of different impact emissions on the overall atmosphere with coupled troposphere–stratosphere. Individual responses of troposphere and stratosphere were not investigated in the present study; however, the stratospheric aerosols would probably have a longer atmospheric lifetime than the tropospheric particles, which settle out quickly[15]. Since some fraction of impact-induced aerosols can reach higher altitudes and be influenced through photochemical processes, the stratosphere and mesosphere/thermosphere coupling following the aftermath of the Chicxulub impact event shall be addressed by further studies.

Data availability

The palaeoclimate general circulation model (GCM) output data as well as the silicate dust grain-size data from the Tanis K-Pg site that support the findings of this study are publicly available in the OSF repository via https://doi.org/10.17605/OSF.IO/2CDQG. The proxy-based latest Cretaceous temperature reconstruction data are available online in the PANGEA repository: https://doi.org/10.1594/PANGAEA.879763.

Code availability

The Python and Matlab source codes developed for reproducing the figures in this study are publicly available at the GitHub repository via github.com/cem-berk-senel/naturegeoscience-chicxulub/. The PlanetWRF model is available upon request from https://planetwrf.com/.

References

51. Toonen, W. H. J. et al. Lower Rhine historical flood magnitudes of the last 450 years reproduced from grain-size measurements of flood deposits using end member modelling. *Catena* **130**, 69–81 (2015).
52. Konert, M. & Vandenberghe, J. E. F. Comparison of laser grain size analysis with pipette and sieve analysis: a solution for the underestimation of the clay fraction. *Sedimentology* **44**, 523–535 (1997).
53. Mahowald, N. et al. The size distribution of desert dust aerosols and its impact on the Earth system. *Aeolian Res.* **15**, 53–71 (2014).
54. Haberle, R. M. et al. Documentation of the NASA/Ames Legacy Mars Global Climate Model: simulations of the present seasonal water cycle. *Icarus* **333**, 130–164 (2019).
55. Li, J. et al. Accounting for dust aerosol size distribution in radiative transfer. *J. Geophys. Res. Atmos.* **120**, 6537–6550 (2015).
56. Leschonski, K. Representation and evaluation of particle size analysis data. *Part. Part. Syst. Charact.* **1**, 89–95 (1984).
57. Richardson, M. I., Toigo, A. D. & Newman, C. E. PlanetWRF: a general purpose, local to global numerical model for planetary atmospheric and climate dynamics. *J. Geophys. Res. Planets* **112**, E09001 (2007).
58. Newman, C. E. et al. Simulating Titan's methane cycle with the TitanWRF general circulation model. *Icarus* **267**, 106–134 (2016).
59. Lee, C. et al. The sensitivity of solsticial pauses to atmospheric ice and dust in the MarsWRF general circulation model. *Icarus* **311**, 23–34 (2018).
60. Temel, O. et al. Large eddy simulations of the Martian convective boundary layer: towards developing a new planetary boundary layer scheme. *Atmos. Res.* **250**, 105381 (2021).
61. Senel, C. B. et al. Interannual, seasonal and regional variations in the Martian convective boundary layer derived from GCM simulations with a semi-interactive dust transport model. *J. Geophys. Res. Planets* **126**, e2021JE006965 (2021).
62. Skamarock, W. C. et al. *A Description of the Advanced Research WRF Version 3* (No. NCAR/TN-475+STR) (University Corporation for Atmospheric Research. 2008).
63. Chou, M.-D. & Suarez, M. J. *A Solar Radiation Parameterization for Atmospheric Studies* Technical Report 104606, Vol. 15 (NASA, 1999).
64. Chou, M.-D. et al. *A Thermal Infrared Radiation Parameterization for Atmospheric Studies* Technical Report 104606, Vol. 19 (NASA, 2001).
65. Feichter, J. et al. Simulation of the tropospheric sulfur cycle in a global climate model. *Atmos. Environ.* **30**, 1693–1707 (1996).
66. Feng, Q., Cui, S. & Zhao, W. Effect of particle shape on dust shortwave direct radiative forcing calculations based on MODIS observations for a case study. *Adv. Atmos. Sci.* **32**, 1266–1276 (2015).
67. Dufresne, J.-L. et al. Longwave scattering effects of mineral aerosols. *J. Atmos. Sci.* **59**, 1959–1966 (2002).
68. Hess, M., Koepke, P. & Schult, I. Optical properties of aerosols and clouds: the software package OPAC. *Bull. Am. Meteorol. Soc.* **79**, 831–844 (1998).
69. Binkowski, F. S. & Shankar, U. The regional particulate matter model: 1. Model description and preliminary results. *J. Geophys. Res. Atmos.* **100**, 26191–26209 (1995).
70. Zhang, L., Gong, S., Padro, J. & Barrie, L. A size-segregated particle dry deposition scheme for an atmospheric aerosol module. *Atmos. Environ.* **35**, 549–560 (2001).
71. Zhang, J. & Shao, Y. A new parameterization of particle dry deposition over rough surfaces. *Atmos. Chem. Phys.* **14**, 12429–12440 (2014).
72. Emerson, E. W. et al. Revisiting particle dry deposition and its role in radiative effect estimates. *Proc. Natl Acad. Sci. USA* **117**, 26076–26082 (2020).
73. Xu, Y. & Carmichael, G. R. Modeling the dry deposition velocity of sulfur dioxide and sulfate in Asia. *J. Appl. Meteorol. Climatol.* **37**, 1084–1099 (1998).
74. Feichter, J., Brost, R. A. & Heimann, M. Three-dimensional modeling of the concentration and deposition of ^{210}Pb aerosols. *J. Geophys. Res. Atmos.* **96**, 22447–22460 (1991).
75. Seinfeld, J. & Pandis, S. N. *Atmospheric Chemistry and Physics: From Air Pollution to Climate Change* (John Wiley & Sons, 2016).
76. Tsarpalis, K. et al. The implementation of a mineral dust wet deposition scheme in the GOCART-AFWA module of the WRF model. *Remote Sens.* **10**, 1595 (2018).
77. Shao, Y. Simplification of a dust emission scheme and comparison with data. *J. Geophys. Res. Atmos.* **109**, D10202 (2004).

78. Shao, Y. et al. Parameterization of size-resolved dust emission and validation with measurements. *J. Geophys. Res. Atmos.* **116**, D08203 (2011).

79. Liu, X. et al. Toward a minimal representation of aerosols in climate models: description and evaluation in the Community Atmosphere Model CAM5. *Geosci. Model Dev.* **5**, 709–739 (2012).

80. Dudhia, J. A multilayer soil temperature model for MM5. In *Sixth PSU/NCAR Mesoscale Model Users' Workshop.* 49–50 (1996).

81. Chen, S.-H. & Sun, W.-Y. A one-dimensional time dependent cloud model. *J. Meteorol. Soc. Jpn. 2* **80**, 99–118 (2002).

82. Tiedtke, M. A comprehensive mass flux scheme for cumulus parameterization in large-scale models. *Mon. Weather Rev.* **117**, 1779–1800 (1989).

83. Zhang, C., Wang, Y. & Hamilton, K. Improved representation of boundary layer clouds over the southeast Pacific in ARW-WRF using a modified Tiedtke cumulus parameterization scheme. *Mon. Weather Rev.* **139**, 3489–3513 (2011).

84. Senel, C. B. et al. A new planetary boundary layer scheme based on LES: application to the XPIA campaign. *J. Adv. Model. Earth Syst.* **11**, 2655–2679 (2019).

85. Jimenez, P. A. et al. A revised scheme for the WRF surface layer formulation. *Mon. Weather Rev.* **140**, 898–918 (2012).

86. Pollard, R. T., Rhines, P. B. & Thompson, R. The deepening of the wind-mixed layer. *Geophys. Fluid Dyn.* **4**, 381–404 (1973).

87. Davis, C. et al. Prediction of landfalling hurricanes with the advanced hurricane WRF model. *Mon. Weather Rev.* **136**, 1990–2005 (2008).

88. Pierrehumbert, R. & Gaidos, E. Hydrogen greenhouse planets beyond the habitable zone. *Astrophys. J. Lett.* **734**, L13 (2011).

89. Su, W., Charlock, T. P., Rose, F. G. & Rutan, D. Photosynthetically active radiation from clouds and the Earth's Radiant Energy System (CERES) products. *J. Geophys. Res. Biogeosci.* **112**, G02022 (2007).

90. García-Rodríguez, A. et al. Modelling photosynthetic active radiation (PAR) through meteorological indices under all sky conditions. *Agric. For. Meteorol.* **310**, 108627 (2021).

91. Hatzianastassiou, N. et al. Ten year radiation budget of the earth: 1984–93. *Int. J. Climatol.* **24**, 1785–1802 (2004).

92. Khoder, M. I. Atmospheric conversion of sulfur dioxide to particulate sulfate and nitrogen dioxide to particulate nitrate and gaseous nitric acid in an urban area. *Chemosphere* **49**, 675–684 (2002).

93. Loftus, K., Wordsworth, R. D. & Morley, C. V. Sulfate aerosol hazes and SO_2 gas as constraints on rocky exoplanets' surface liquid water. *Astrophys. J.* **887**, 231 (2019).

94. Gulick, S. et al. Importance of pre-impact crustal structure for the asymmetry of the Chicxulub impact crater. *Nat. Geosci.* **1**, 131–135 (2008).

95. Bekki, S. Oxidation of volcanic SO_2: a sink for stratospheric OH and H_2O. *Geophys. Res. Lett.* **22**, 913–916 (1995).

96. Ohno, S. et al. Production of sulphate-rich vapour during the Chicxulub impact and implications for ocean acidification. *Nat. Geosci.* **7**, 279–282 (2014).

Author contributions

C.B.S. and P.K. led the writing of the paper. C.B.S., P.K., O.T., J.V., S.G., P.C. and Ö.K. built the conceptualization of study and wrote the original text. C.B.S., P.K., O.T., J.V., S.G., R.D., M.A.P., P.C. and Ö.K. commented on and edited the original and revised manuscripts. C.B.S., O.T. and Ö.K. developed the general circulation model, implemented microphysics and radiation models and performed palaeoclimate simulations and post-processing of the results. P.K. and R.D. collected sediment samples during fieldwork at the Tanis K-Pg site in August 2017. P.K. carried out laser-diffraction grain-size analyses, with lab supervision of M.A.P. P.K. created Figs. 1 and 2 and Extended Data Fig. 1. C.B.S. created all other figures. All authors approved the final draft of the manuscript.

Competing interests

The authors declare no competing interests.

Additional information

Extended data is available for this paper at https://doi.org/10.1038/s41561-023-01290-4.

Supplementary information The online version contains supplementary material available at https://doi.org/10.1038/s41561-023-01290-4.

Correspondence and requests for materials should be addressed to Cem Berk Senel.
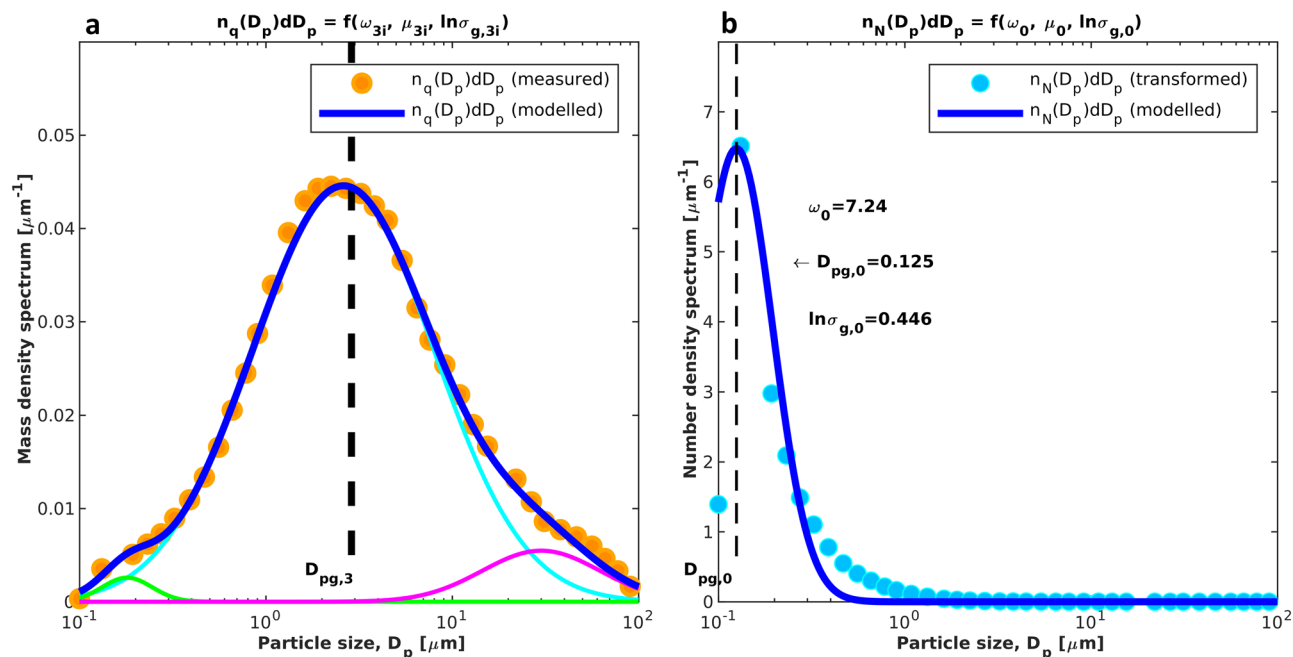
Peer review information *Nature Geoscience* thanks Teruyuki Maruoka, Julia Brugger and the other, anonymous, reviewer(s) for their contribution to the peer review of this work. Primary Handling Editor: Tamara Goldin, in collaboration with the *Nature Geoscience* team.

Reprints and permissions information is available at www.nature.com/reprints.
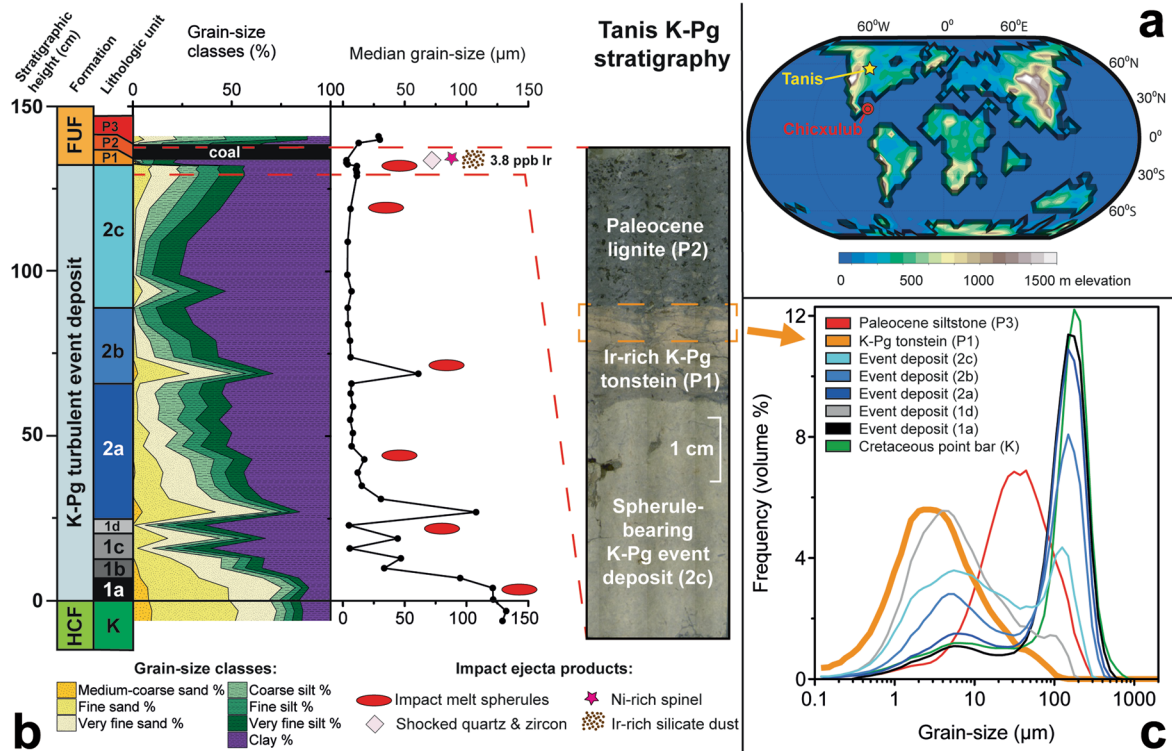
Extended Data Fig. 1 | Geological context of the Chicxulub impact ejecta stratigraphy at the Tanis K-Pg boundary site. a The inset shows a paleogeographic reconstruction and relief map for the latest Cretaceous[42] as used in this modeling study with locations of Chicxulub and Tanis indicated. The base map is based on the latest Cretaceous paleogeographic data[42]. **b** Stratigraphy of the Tanis K-Pg boundary event deposit highlighting the lithological units (adapted from[41]; based on sections X-2741-A and X-2761) together with data on grain-size classes (clay, silt, and sand fractions), median grain-size values (in µm) and different types of impact ejecta found within this deposit. HCF = Hell Creek Formation (Upper Cretaceous). FUF = Fort Union Formation (Paleocene). **c** Representative grain-size distribution curves throughout the section, the colors match the stratigraphic units in b. The uppermost K-Pg boundary claystone (unit P1), indicated with a bold orange line, corresponds to final phases of atmospheric fallout of silicate dust injected by the impact and is used in present GCM simulations.

a $n_q(D_p)dD_p = f(\omega_{3i}, \mu_{3i}, \ln\sigma_{g,3i})$

b $n_N(D_p)dD_p = f(\omega_0, \mu_0, \ln\sigma_{g,0})$

$\omega_0 = 7.24$

$\leftarrow D_{pg,0} = 0.125$

$\ln\sigma_{g,0} = 0.446$

Extended Data Fig. 2 | Mass and number density spectra of the grain-size dataset. a Mass density spectrum of Tanis sediment sample X-2761-8A displayed by filled orange circles, which corresponds to the uppermost K-Pg claystone interval just below a Paleocene lignite and yields a median grain-size of 2.88 μm. The measured mass density spectrum was fitted by a trimodal lognormal size distribution as depicted by the blue solid line. This fitted model curve is the sum of lognormal size distributions comprising 3 modes. Model parameters

are as follows: $w_0 = 0.002$, $D_{pg,0} = 0.18$ μm, $\ln\sigma g,0 = 0.3087$ (mode 1, green solid line), $w_0 = 0.125$, $D_{pg,0} = 2.6$ μm, $\ln_{\sigma g,0} = 1.1193$ (mode 2, cyan solid line), $w_0 = 0.01$, $D_{pg,0} = 30$ μm, $\ln_{\sigma g,0} = 0.7284$ (mode 3, magenta solid line), **b** Converted grain-size distribution into number density spectrum displayed by filled cyan circles. The converted spectrum is fitted by a lognormal size distribution (blue solid line), which is the input parameter for our GCM study. Converted model median grain-size corresponds to 0.125 μm with a logarithmic standard deviation of 0.446.
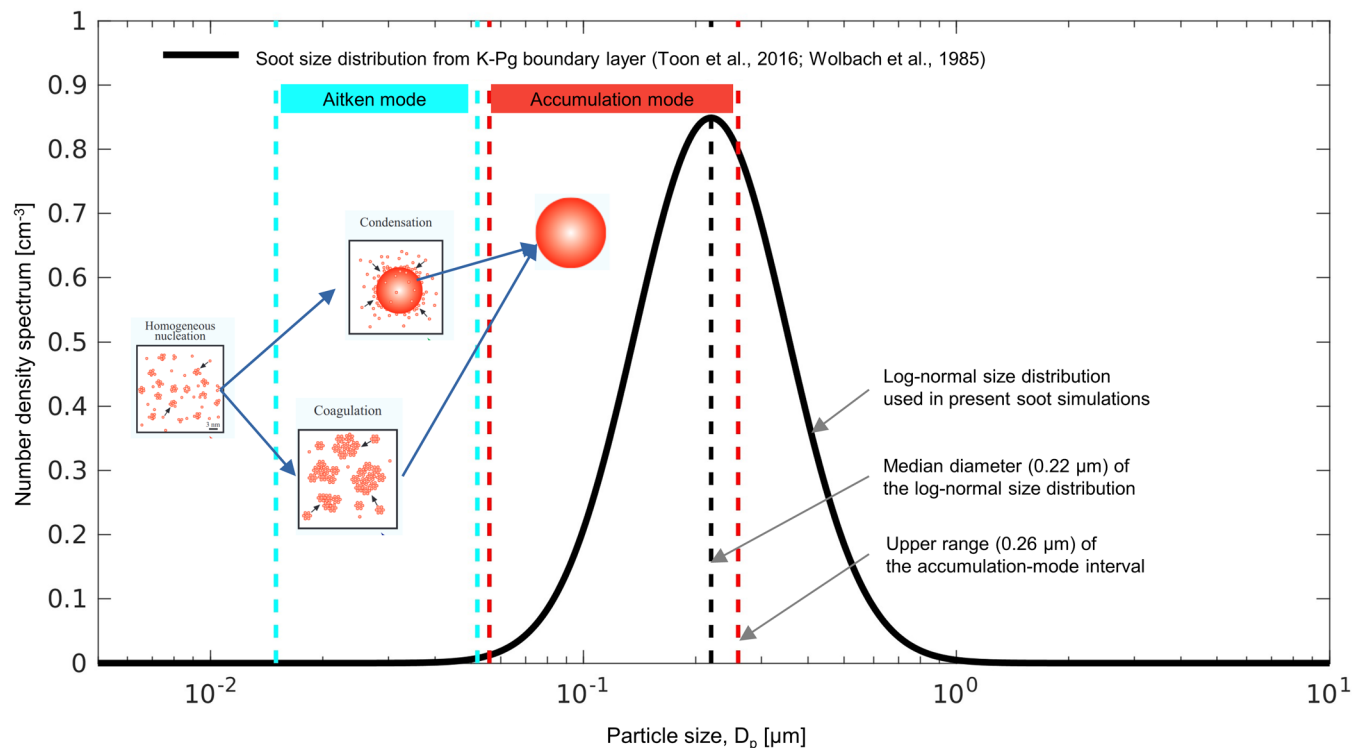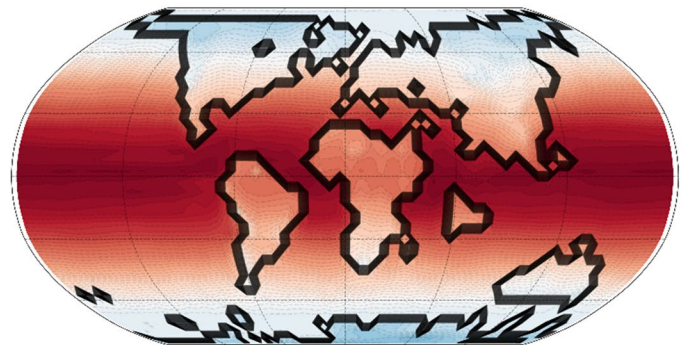
Extended Data Fig. 3 | Number density spectrum of soot along with the particle size from K-Pg boundary layer. It indicates a median diameter of 0.22 μm (Toon et al., 2016[39]; Wolbach et al., 1985[20]). Concerning the aerosol life cycle and processes, coagulation is one of the crucial microphysical mechanisms that might pose as important for the transport of aerosols in the atmosphere. Nanometric particles below 0.1 μm, that is, 0.015 μm < D_p < 0.052 μm[79], whose range is referred to as the Aitken-mode (within the cyan dashed lines), are formed by two processes: (i) condensational growth on existing aerosol particles,

and (ii) coagulation due to the random particle collisions. These nanometric particles can further grow into larger particles or chains, resulting in the so-called accumulation-mode (0.056 μm < D_p < 0.26 μm)[79] (within the red dashed lines) where the coagulation can occur especially at high particle concentrations following the K-Pg impact. The median diameter of soot (0.22 μm[20,39]) in our simulations are prominently larger than the Aitken-mode interval, while lying within the range of accumulation-mode.
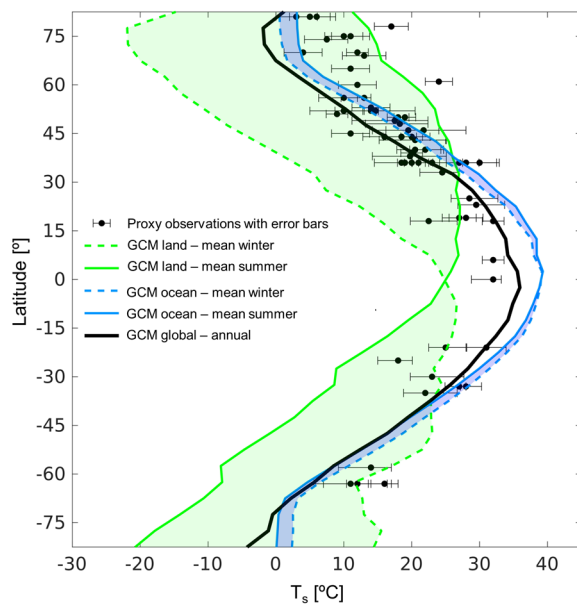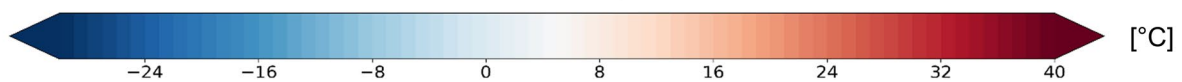
Extended Data Fig. 4 | Latest Cretaceous surface temperatures from our GCM simulations, one year before the impact, in comparison with proxy observations[43]**.** Proxy temperature data are presented as mean values +/- standard error of mean (SEM), displayed by black circles and horizontal error bars. Here, the proxy data consists of N = 66 samples at different latitudes. Green solid and dashed lines display the zonal mean of land temperatures during the boreal summer and winter seasons, from GCM simulations. Blue solid (boreal summer) and dashed (boreal winter) lines indicate the zonal mean of ocean temperatures. Both green (land) and blue (ocean) shaded areas show the region between the mean boreal summer and winter profiles. The black solid line refers to the GCM-based annual average of land and ocean surface temperatures at each latitude.

Extended Data Fig. 5 | Global surface temperature reconstructions using the combined fine-grained ejecta scenario. Results are displayed on a latest Cretaceous paleogeographic map (Extended Data Fig. 1a) and shown for different time snapshots. **a** Latest Cretaceous, 1 year before impact (annual mean). **b** Latest Cretaceous, 1 week before impact. **c** Impact winter, 1 month after impact. **d** 6 months after impact. **e** 2 years after impact. **f** 10 years after impact (annual-mean). Base maps are based on the latest Cretaceous paleogeographic data[42].
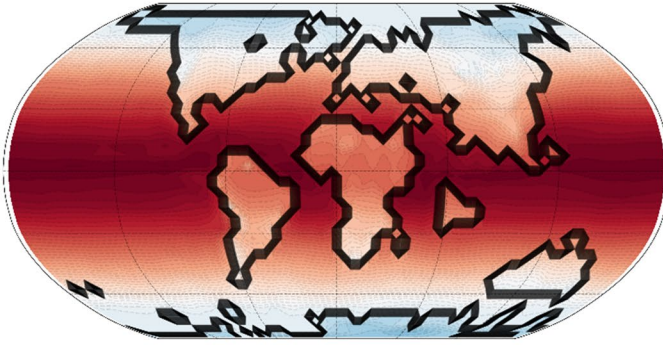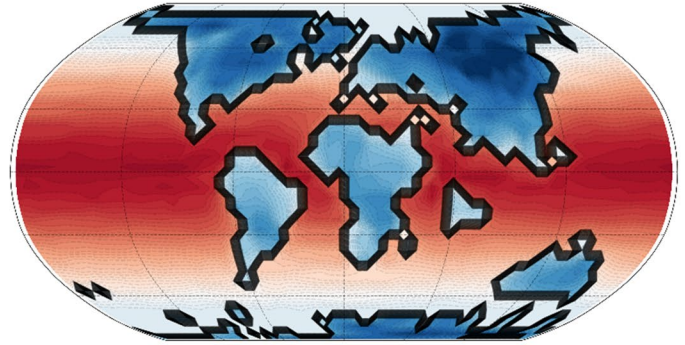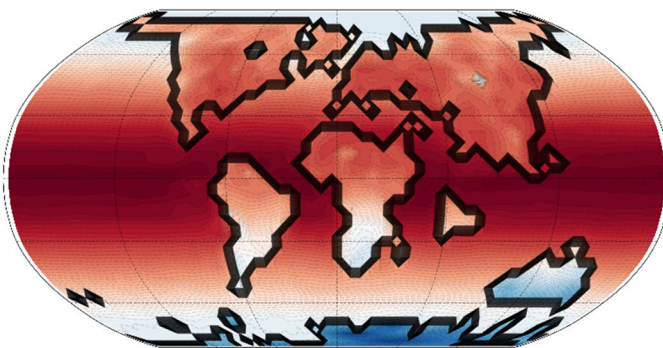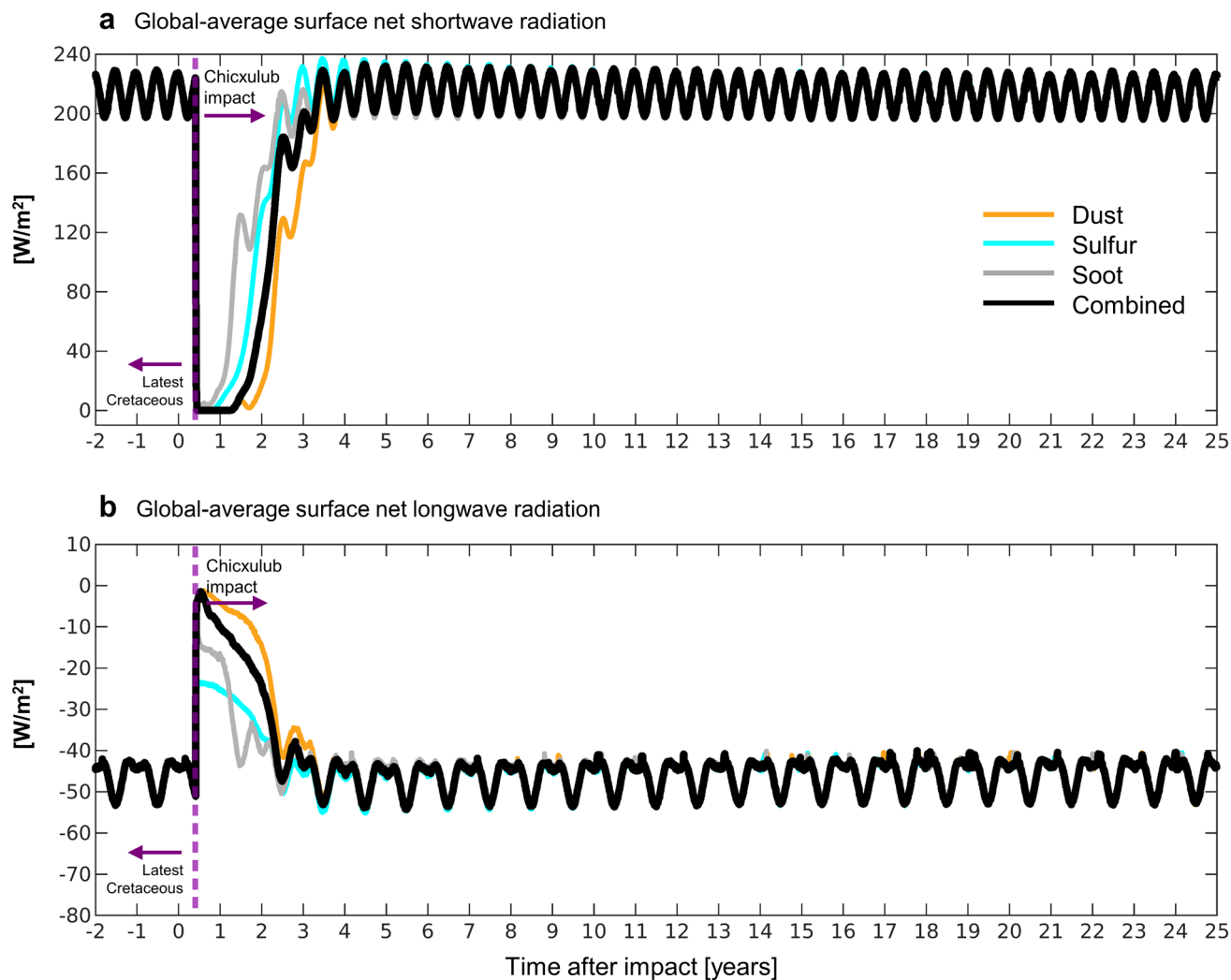
Extended Data Fig. 6 | Impact-generated global surface net radiative responses. The temporal evolution from −2 years of the latest Cretaceous towards 25 years of post-impact conditions, for the individual silicate dust, sulfur, soot, and combined scenarios. **a** Global-average surface net shortwave radiation flux. **b** Global-average surface net longwave radiation flux. Here in x-axis, the year of 0 refers to the start of the year where the impact event occurs. The solid purple dashed line denotes the moment of Chicxulub impact, that is, boreal spring season[38]. Our paleoclimate simulations indicate that the drastic changes in surface net shortwave/longwave radiation stabilize to pre-impact levels within the first 3 years after impact. Accordingly, this timescale, in which large radiative anomalies emerged, determines the timescale of the initial extreme cold (Fig. 4a).

**a** Latest Cretaceous: 1 day before impact (boreal spring)
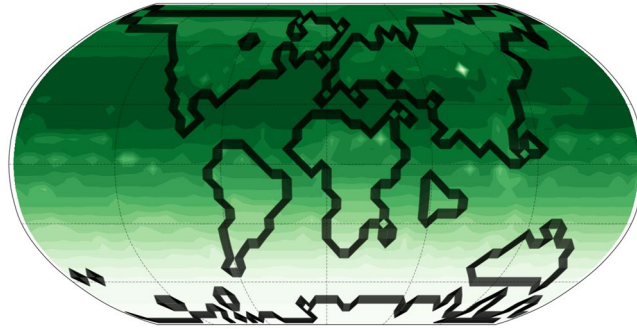
b Latest Cretaceous: 6 months before impact (austral summer)

Global photosynthetic active radiation [W/m²]

0   20   40   60   80   100   120   140   160
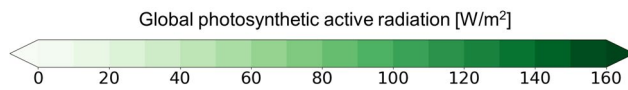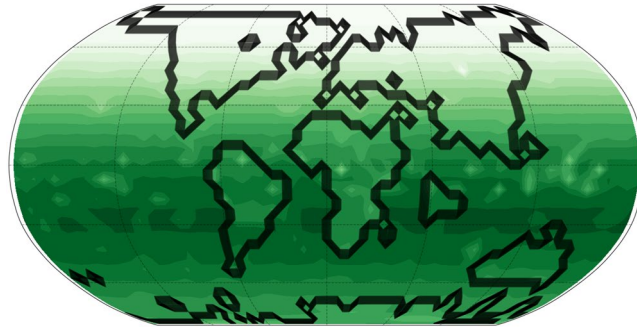
Extended Data Fig. 7 | Global PAR flux reconstructions in the latest Cretaceous. Land-Ocean PAR flux **a** 1 day before impact (boreal spring) and **b** 6 months before impact (austral summer), displayed on a latest Cretaceous paleogeographic map (Extended Data Fig. 1a). The range of the green and purple colorbar represents the photosynthetically high and low radiative flux, varying between 0-160 W/m². Base maps are based on the latest Cretaceous paleogeographic data[42].
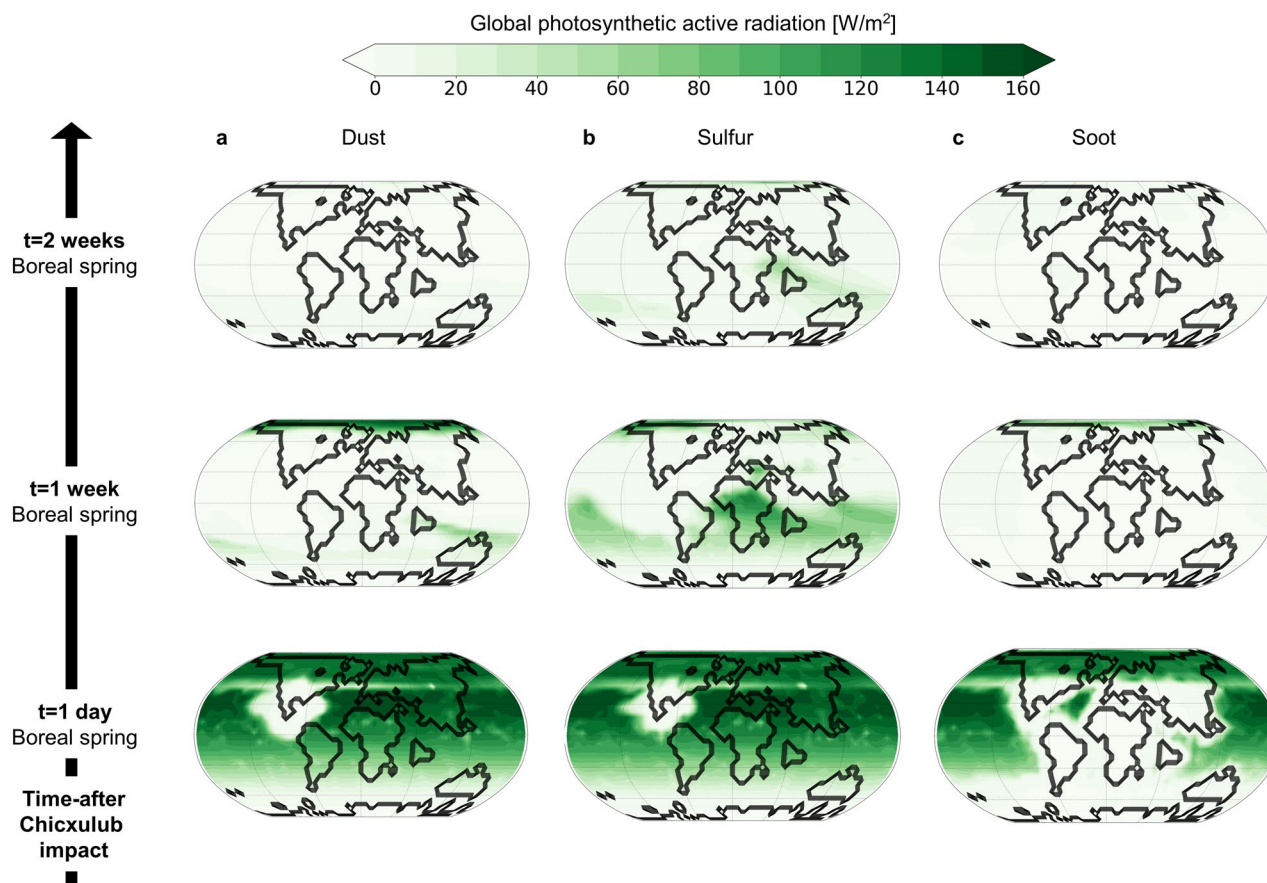
Extended Data Fig. 8 | PAR flux reconstructions following the Chicxulub impact. Land and ocean PAR flux from 1 day (post-impact state, instantaneous) to 1 and 2 weeks after impact for **a** silicate dust; **b** sulfur; and **c** soot scenarios, displayed on a latest Cretaceous paleogeographic map (Extended Data Fig. 1a). The range of the green-white colorbar denotes the photosynthetically high and low radiative flux. Base maps are based on the latest Cretaceous paleogeographic data[42].
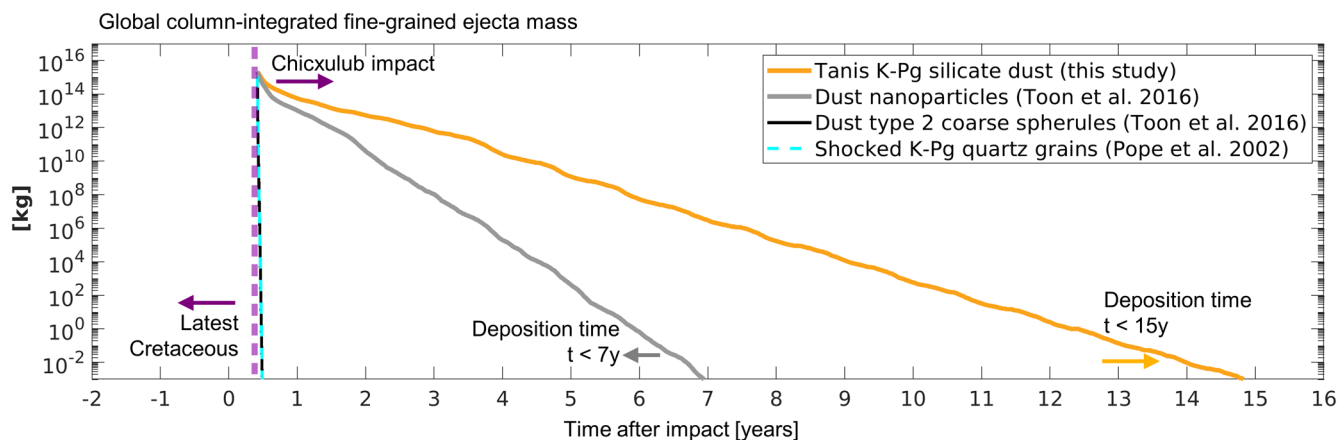
Extended Data Fig. 9 | Effect of silicate dust particle size on the global column-integrated fine-grained ejecta mass. Orange line refers to the present study, using the Tanis K-Pg silicate dust. Gray and black lines show GCM results using particle size constraints reported in previous modeling studies[18,39]. The gray line displays the response of nanometric sized particles, indicating a deposition rate with an atmospheric lifetime of ~7 years (as a lower threshold). The black line refers to the type 2 spherules[39], representing microkrystites of 250 μm in diameter prone to very swift gravitational settling within a few days after impact. Cyan dashed line displays the shocked ejected quartz grains (mean diameter of 50 μm) defined as clastic debris[27]. We use the same amount of ejecta release in each GCM simulation, in the order of 2×10^{18} g as an upper limit. The optical properties of nanoparticles and type 2 spherules are the same as in the Tanis K-Pg silicate dust simulation, as we compare the microphysical response to the changes in particle size. Here in x-axis, the year of 0 refers to the start of the year where the impact event occurs. The purple dashed line denotes the moment of Chicxulub impact, that is, boreal spring season[38]. Regarding nanoparticles, those nanometric sized particles (median diameter of 20 nm) would grow into larger particles in atmosphere due to the coagulation. Such larger aggregates would have lower deposition rates on land and ocean (Fig. 3), hence higher atmospheric lifetimes. To illustrate, the deposition rate of nanoparticles (gray dashed line) would have occasionally shifted rightward through the response of silicate dust (orange dashed line) depending on the rate of coagulation. Therefore, the present simulation of nanoparticles, excluding coagulation, would serve as the minimum threshold for the atmospheric lifetime (t ~ 7 years). The inclusion of coagulation mechanism forming larger aggregates would lead to lower deposition rates on land and ocean (Fig. 3) for some fraction of nanoparticles, thus relatively high atmospheric lifetime of more than 7 years. Nevertheless, we do not expect nanoparticles to have an atmospheric lifetime and PAR response as substantial as single soot or micrometer-sized silicate dust.
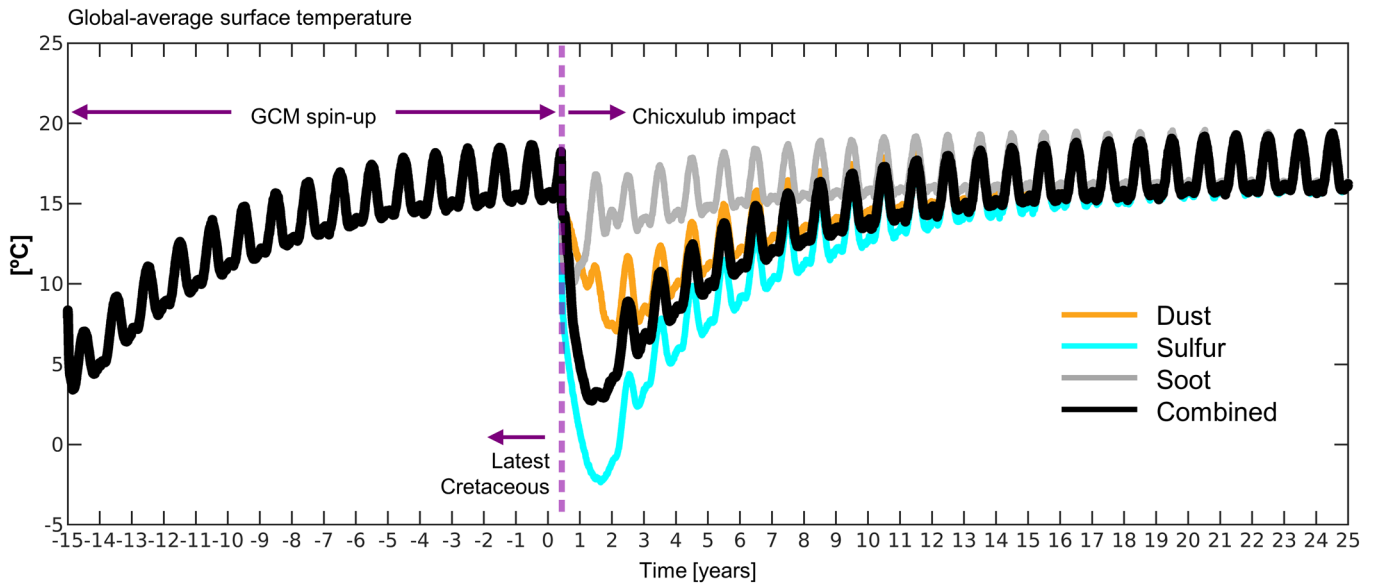
Extended Data Fig. 10 | Global-average surface temperature. It is same as Fig. 4a, yet the time evolution is shown from 15 years before the Chicxulub impact instead of 2 years, for the individual silicate dust, sulfur, soot, and combined scenarios. The first 15 years correspond to the model initial spin-up simulation of 15-years, in which the latest Cretaceous conditions stabilized.